Chemical Engineering Journal Advances 22 (2025) 100744

Contents lists available at ScienceDirect

Chemical Engineering Journal Advances

journal homepage: www.sciencedirect.com/journal/chemical-engineering-journal-advances

Lagrangian Sensor Particles for detecting hydrodynamic heterogeneities in industrial bioreactors: Experimental analysis and Lattice-Boltzmann simulations

Sebastian Hofmann [a,*], Ryan Rautenbach [a], Lukas Buntkiel [b], Isabel Sophie Brouwers [a], Lena Gaugler [c], Jonas Barczyk [c], Jürgen Fitschen [d], Sebastian Reinecke [b], Marko Hoffmann [a], Ralf Takors [c], Uwe Hampel [b,e], Michael Schlüter [a]

[a] Institute of Multiphase Flows, Hamburg University of Technology, Eißendorfer Str. 38, 21073 Hamburg, Germany
[b] Helmholtz-Zentrum Dresden-Rossendorf, Bautzner Landstraße 400, 01328 Dresden, Germany
[c] Institute of Biochemical Engineering, University of Stuttgart, Allmandring 31, 70569 Stuttgart, Germany
[d] Late Stage USP Development, Bioprocess Development Biologicals, Boehringer Ingelheim Pharma GmbH & Co. KG, Germany
[e] Chair of Imaging Techniques in Energy and Process Engineering, Dresden University of Technology, 01062 Dresden, Germany

ARTICLE INFO

Dataset link: Gitlab project, DaRUS repository

Keywords:
Lagrangian Sensor Particles
Resolved particle Lattice-Boltzmann large eddy simulation
Industrial-scale stirred tank reactor
Compartments
Global and local mixing time

ABSTRACT

This study analyzes trajectories of three particle types in an industrial-scale bioreactor, equipped with a Rushton turbine and a pitched blade turbine, to characterize hydrodynamic compartments. The trajectories obtained from measurements with Lagrangian Sensor Particles (*LSP,exp*) are compared to those generated by Lattice-Boltzmann large eddy simulations (LB LES). The latter method is used to reproduce analogous simulated LSPs (*LSP,sim*) as resolved particles. Additionally, for benchmarking purposes, massless tracer particles (*tracer,sim*) are incorporated to accurately represent fluid flow dynamics. Discrepancies in the axial probability of presence and velocity between *LSP,exp* and *LSP,sim* likely stem from differences in mass distribution, density, number of particles, and ratio of particle size to grid. A necessarily high *LSP,sim* volume fraction in LB LES leads to increased collisions and clustering, negatively impacting flow dynamics, and reducing turbulent kinetic energy by at least 3%. Circulation and residence time distributions for the three types of particles identify three hydrodynamic compartments within the bioreactor, validated by local mixing time distributions. The ratio of overall average circulation time to global mixing time is $\Theta_{\mathrm{glob,95}} \approx 3.0 \cdot \bar{t}_{\mathrm{circ}}$ for *LSP,exp*, which largely corresponds to literature results. A theoretical LSP size of $d_{\mathrm{p,th}} \approx 1\,\mathrm{mm}$ is estimated to be flow following on micro-scale in the bulk phase, if a Stokes number of $St = 0.1$ is assumed. However, Stokes number estimations confirm that *LSP,exp* are capable to follow flow patterns on the meso-scale and macro-scale with $St \approx 0.2$ and $St \approx 0.002$, respectively. Hence, hydrodynamic structures at length scales greater than or equal to the size of the impeller can be investigated by current state-of-the-art LSPs, which proves their technological readiness for industrial bioreactors.

1. Introduction

For industrial biopharmaceutical production, stirred tank reactors (STR) are essential. The characterization and process monitoring of such reactors is generally limited to traditional Eulerian wall-mounted probes, which measure process conditions such as temperature, pH, conductivity, oxygen, and many more. However, the downside of such probes is that they are locally fixed and do not represent the entirety of the reactor volume.

On an industrial scale, heterogeneities in the form of compartments [1] occur and have adverse effects on the dynamics of the cell cycle and energy levels when exposed to strong fluctuations in the media during mixing [2–4]. Mixing times, ranging from approximately ten seconds and longer, exceed the duration of key intracellular processes and, consequently, may lead to population heterogeneity. The extent depends on the severity and time scale to which the cell is exposed to gradients in repeatedly unpredictable microenvironments [5–7]. This issue becomes even more complex when existing production processes are intensified using perfusion systems [8], or when novel bioprocesses are developed with artificial microbial consortia [9–12]. From

* Corresponding author.
E-mail addresses: sebastian.hofmann@tuhh.de (S. Hofmann), michael.schlueter@tuhh.de (M. Schlüter).

https://doi.org/10.1016/j.ceja.2025.100744
Received 13 January 2025; Received in revised form 28 March 2025; Accepted 31 March 2025
Available online 19 April 2025

Nomenclature

Arabic symbols

$\dot{V}_j$	Volume flow rate in reactor slice j / $m^3\,s^{-1}$
$\bar{t}_{circ,overall}$	Overall average circulation time / s
$\tilde{d}_{travel}$	Maximum traveled distances / m
$\boldsymbol{c}_i$	Finite velocity in discrete lattice D3Q19 / $m\,s^{-1}$
$\boldsymbol{F}_{ext}$	External forces / N
$\boldsymbol{u}'$	Fluid velocity fluctuation / $m\,s^{-1}$
$\boldsymbol{u}'_{rms,sim}$	Root mean square of simulated fluid velocity fluctuations / $m\,s^{-1}$
$\boldsymbol{u}_{stoch}$	Stochastic fluid velocity fluctuation magnitude / $m\,s^{-1}$
$\boldsymbol{v}'$	Particle velocity fluctuation / $m\,s^{-1}$
$\boldsymbol{V}_{slip,stoch}$	Stochastic slip velocity / $m\,s^{-1}$
A_j	Surface area of reactor slice j / m^2
B	Fitting constant / –
b	Baffle width / m
C	Impeller off-bottom clearance / m
c_D	Drag coefficient / –
C_s	Smagorinsky coefficient / –
Co	Courant number / –
d_{imp}	Impeller diameter / m
d_{LSP}	LSP diameter / m
$d_{p,th,MF}$	Theoretical maximum particle diameter in mean flow/ m
$d_{p,th,stoch}$	Theoretical maximum particle diameter, stochastically / m
d_p	Particle diameter / m
d_{STR}	Reactor diameter / m
f	Particle distribution function / $m^{-6}\,s^3$
f^{eq}	Equilibrium particle distribution density / $m^{-6}\,s^3$
H	Reactor filling height / m
h	Impeller spacing / m
h_j	Height of reactor slice j / m
I'_t	Normalized gray scale intensity over time / –
k	Turbulent kinetic energy / $m^2\,s^{-2}$
L	Characteristic fluid flow length scale / m
L_E	Taylor scale / m
L_{MF}	Flow length scale of the mean flow / m
M	Total trials per rpm case / –
m_{LSP}	LSP mass / kg
n	Impeller frequency / rpm
N_{imp}	Number of impellers / –
$N_{LSP,sim}$	Number of simulated LSPs in reactor / –
N_j	Number of counts in bin j / –
P	Global power input / W
P	Probability / –
p	Hydrostatic pressure / Pa
$P\,V^{-1}$	Global power per volume input / $W\,m^{-3}$
p_0	Ambient pressure / Pa
p_{res}	Pressure resolution / Pa
PCP	Particle collision or perturbation probability / %
Po	Power number / –
r_{imp}	Impeller radius / m
r_{shift}	Center of mass offset / mm
Re_{STR}	Stirrer Reynolds number / –
Re_p	Particle Reynolds number / –
St	Stokes number / –
St_{MF}	Stokes number of the mean flow / –
St_{stoch}	Stochastic Stokes number / –
T	Temperature / °C
t_{circ}	Circulation time / s
$t_{rec,single,exp}$	Recording time of single experimental LSP / s
$t_{sim,max}$	Maximum physical simulated time per particle / s
$t_{rec,tot,exp}$	Total recording time of experimental LSPs per rpm case / h
$t_{rec,tot,sim}$	Total recording time of simulated particles per rpm case / h
u	Velocity of the fluid / $m\,s^{-1}$
u_{tip}	Impeller tip speed / $m\,s^{-1}$
V	Reactor working volume / m^3
v	Velocity of the LSP / $m\,s^{-1}$
$v_{z,max}$	Maximum axial velocity / $m\,s^{-1}$
v_z	Axial velocity / $m\,s^{-1}$
w	Weight for average value / –
w_G^0	Superficial gas velocity / $mm\,s^{-1}$
z	Specific height in reactor / m
$z\,H^{-1}$	Normalized reactor height / –

Greek symbols

Δ	Uncertainty
Δx	Lattice spacing in numerical simulations / m
η	Dynamic viscosity / Pa s
γ	Linear correlation coefficient / –
Λ	Turbulence length scale / m
λ_K	Kolmogorov length scale / m
$\lambda_{K,\phi}$	Min. Kolmogorov length scale / m
$\mathcal{O}$	Magnitude / –
ν	Kinematic viscosity / $m^2\,s^{-1}$
Ω	Collision parameter / $m^{-6}s^2$
$\bar{\tau}_{overall}$	Overall cumulative residence time / s
ϕ	Local energy dissipation ratio / –
$\Phi_{LSP,exp}$	Experimental LSP volume fraction / –
$\Phi_{LSP,sim}$	Experimental LSP volume fraction / –
ρ	Density / $kg\,m^{-3}$
ρ_f	Fluid density / $kg\,m^{-3}$
ρ_p	Particle density / $kg\,m^{-3}$
σ^2	Intensity variance / –
τ	Residence time / s
τ_c	Collision time / s

a hydrodynamic point of view, the entire reactor shows a substantial variation of energy dissipation rates and resulting Kolmogorov length scales, which may additionally decrease the quality and quantity of the product [13,14].

In this case, numerical simulations support the identification of metabolic regimes in the STR and are able to perform a lifeline analysis for occurring mass transfer limitations [15–17]. Eventually, these

τ_{regime}	Residence time per hydrodynamic regime / s
τ_f	Characteristic time of the flow field / s
τ_p	Particle response time / s
Θ^*	Relative local mixing time / s
$\Theta_{glob,95}$	Global mixing time / s
$\Theta_{loc,95}$	Local mixing time / s
$\varepsilon_{T,loc}$	Local energy dissipation rate / $W\,kg^{-1}$
ε_T	Energy dissipation rate / $W\,kg^{-1}$
ζ	Continuous velocity of particles / $m\,s^{-1}$

Abbreviations

4D-PTV	4D-Particle Tracking Velocimetry
BTB	Bromothymol blue
CHO	Chinese Hamster Ovary
CTD	Circulation time distribution
D3Q19	Lattice-Boltzmann lattice structure
DW	Deionized water
exp	Experimental
GPU	Graphical processor unit
HCl	Hydrochloric acid
HZDR	Helmholtz-Zentrum Dresden-Rossendorf
IMU	Inertial Measurement Unit
IPO	Injection point
LB LES	Lattice-Boltzmann large eddy simulations
LED	Light Emitting Diode
LP	Lagrangian Particle
LSP,exp	Experimental LSPs
LSP,sim	Simulated LSPs
LSP	Lagrangian Sensor Particle
LX 500	Lattice points across reactor diameter
mag	Magnitude
MF	Mean flow
NaCl	Sodium chloride
NaOH	Sodium hydroxide
PBT-6	6-bladed Pitched blade turbine
PDF	Probability density function
rms	Root mean square
RT-6	6-bladed Rushton turbine
RTD	Residence time distribution
sim	Simulated
stoch	Stochastic
STR	Stirred Tank Reactor
TKE	Turbulent kinetic energy
tracer,sim	Simulated tracer particles

combined analyzes are utilized for modeling scale-down bioreactors to understand large-scale phenomena on a laboratory scale, improve process parameters, and predict product outcomes when scaling back up. It enables the investigation of cell-bioreactor interactions with high flexibility through various concepts and stress responses [18–21]. However, numerical simulations have a limitation in accurately predicting realistic bubble size distributions for dense bubbly flows in industrial-sized bioreactors. Applying highly resolved simulations to implement bubble breakup [22] and coalescence [23] is very demanding due to the high computational cost [24]. Hence, the cell's metabolic pathway in multiphase flows and subsequent data for scale-down models lack accuracy, since oxygen stress conditions lead to a decrease in production rate [25,26].

This is the reason why experiments on heterogeneities, in particular on an industrial scale, are crucial to deliver further validation data. Therefore, various research groups have developed and successfully implemented Lagrangian Sensor Particles (LSP), which dynamically measure conditions within the STR, while not being locally fixed to the reactor wall [27–29]. The idea is that such an LSP follows the fluid flow in its characteristic way, essentially mimicking the lifeline [2,30,31] of a microorganism during cultivation and providing the desired parameter readings. Recent publications discuss their flow-following capability and its ability to highlight hydrodynamic heterogeneities in an industrial-scale bioreactor [32–34]. However, to what extent such LSPs are flow-following and represent lifelines of a cell deserves to be studied more in detail. Moreover, determining its location using an inertial measurement unit (IMU), and thus achieving a full spatio-temporal resolution over a long period of time, is challenging [29,35,36].

In turn, Lattice-Boltzmann large eddy simulations (LB LES) demonstrate a state-of-the-art methodology for obtaining detailed fluid flow information and transient flow structures in an STR [37–39], and even largely predict the trajectories of small inertial particles in a single-phase system [34,40]. Yet, for the latter, careful consideration must be undertaken, as the particle diameter should not exceed the respective lattice spacing [41]. As soon as the particles reach the size of an LSP and thus are much larger than the lattice spacing, the *resolved discrete element particle* model enhances the capabilities of inertial particles by explicitly resolving the flow field in the boundary layer around the particle and computing associated forces [42]. Eventually, the numerical simulation of LSPs would yield the desired fully resolved spatiotemporal resolution, however, it lacks information on the quality of the trajectories.

To this end, this study compares three particle types: trajectories obtained from measurements with LSPs with replicas from a resolved particle Lattice-Boltzmann large eddy simulation (LB LES) and also massless tracers depicting Chinese Hamster Ovary (CHO) cells in a 15,000 L bioreactor. By doing so, the reactor, which is equipped with a Rushton turbine and a pitched blade turbine, is hydrodynamically characterized, whereupon the compartments and mixing heterogeneities are identified by data gathered via LSPs and validated by experimental mixing time trials. Eventually, a Lagrangian regime analysis and Stokes number estimations provide crucial information about potential oxygen deprivation zones and technological improvements of the reactor system. The ultimate goal of the study is to demonstrate the technological readiness of LSPs and further utilize the information gained to advance the development of scale-down models.

2. Materials and methods

2.1. 15,000 L stirred tank reactor and impellers

The stirred tank reactor (STR) utilized is a replica of an industrial bioreactor, made of acrylic glass, and has been erected in collaboration with Boehringer Ingelheim Pharma GmbH & Co. KG [43]. It is utilized for both experimental investigations and Lattice-Boltzmann large eddy simulations (LB LES). With its inner diameter of $d_{imp} = 2.0\,m$, a dished head at the reactor bottom, and a filling level of $H = 4.27\,m$, the total working volume in this study is $V = 12,500\,L$ (Fig. 1). It is filled with deionized water (DW) at a temperature of $T = (22.0 \pm 0.3)\,°C$ at an estimated viscosity of $\eta = 0.95 \cdot 10^{-3}\,Pa\,s$ and measured densities as described in Table 1 (Anton Paar DMA 35). The STR is equipped with three equally spaced baffles of width $b = 0.1 \cdot d_{STR}$ and a bottom-mounted magnetic agitator (ZETA BMRF XXL) with two impeller stages, namely a six-bladed Rushton turbine (RT-6, first stage) and a six-bladed pitched blade turbine (PBT-6, second stage) with a diameter of $d_{imp} = 0.665\,m$, which corresponds to a ratio of $d_{imp} \cdot d_{STR}^{-1} = 0.33$. The off-bottom clearance is $C = 0.3 \cdot d_{STR}$ and the impellers are spaced at $h \cdot d_{imp}^{-1} = 1.65$. Impeller geometries are also described in Šrom et al. [13].

Table 1
Overview of experimental parameters for deionized water (DW) and Lagrangian Sensor Particles (LSPs).

	Deionized water (DW)
Temperature T / °C	(22 ± 0.3)
Dynamic viscosity η $(\cdot 10^{-3})$ / Pa s	0.95
Fluid density ρ_f / kg m^{-3}	(998.1 ± 0.4)
LSP density ρ_p / kg m^{-3}	$\rho_f \leq \rho_p \leq (\rho_f + 1.0)$

This study evaluates four impeller frequencies n between 32 rpm and 63 rpm (Table 2), which correspond to the respective stirrer Reynolds numbers calculated as

$$Re_{STR} = \frac{\rho_f \, n \, d_{imp}^2}{\eta}. \tag{1}$$

The power input P into an STR caused by the installed impellers turning in a fluid with the density ρ_f is estimated with

$$P = Po \cdot \rho_f \cdot n^3 \cdot d_{imp}^5, \tag{2}$$

which is used to determine the specific power input PV^{-1} containing the STR working volume V. In this study, the power number is estimated to be $Po = 6.5$ for both RT-6 and PBT-6 when used in combination. For biotechnological processes, including the cultivation of Chinese Hamster Ovary (CHO) cells, it is of interest to appraise critical length scales in such an STR to estimate potential cell damage. The most important is the Kolmogorov length scale λ_K, which describes the smallest scale in a turbulent flow and is calculated according to

$$\lambda_K = \left(\frac{\nu^3}{\bar{\varepsilon}_T} \right)^{\frac{1}{4}}, \tag{3}$$

with the kinematic viscosity ν and the mean energy dissipation rate $\bar{\varepsilon}_T$, which is defined for STRs like

$$\bar{\varepsilon}_T = \frac{P}{V \, \rho_f}. \tag{4}$$

Moreover, Ståhl Wernersson and Trägårdh [44] suggested in a scale-independent approach that the highest local energy dissipation rates $\varepsilon_{T,loc}$ occur in the vicinity of the Rushton turbine and thus the length scales must be smaller according to

$$\log(\phi) = \log\left(\frac{\varepsilon_{T,loc}}{\bar{\varepsilon}_T} \right) = -1.04 \cdot \left(\frac{2 \cdot r_{imp}}{d_{imp}} \right) + 3.10, \tag{5}$$

where ϕ is the ratio between $\varepsilon_{T,loc}$ and $\bar{\varepsilon}_T$. In that case, the maximum value would occur with the radius $r_{imp} = 0.5 \cdot d_{imp}$ directly at the edge of the impeller, which is equal to $\phi = 114.8$ and would result in lower Kolmogorov length scales $\lambda_{K,\phi=115}$ (Table 2). Most recently, Šrom et al. report of $\phi = 4114$ in the same reactor setup, measured experimentally [13]. Literature findings suggest that cell damage is unlikely to occur if the Kolmogorov length scale exceeds the size of the respective cultivated cell, such as a CHO cell between 12 and 14 µm in diameter [14,45,46].

Another length scale used in this study is the Taylor scale

$$L_E = u'_{rms,sim} \cdot \sqrt{\frac{15\,\nu}{\bar{\varepsilon}_T}}, \tag{6}$$

which helps to roughly estimate the size of the smallest eddies [47] with $u'_{rms,sim}$ being the root mean square of the fluid velocity fluctuations [48], which is taken from the numerical simulations and being roughly a tenth of the tip speed $u'_{rms,sim} = 0.1 \cdot u_{tip}$ [32] (Table 2).

2.2. Lagrangian sensor particles

The spherical Lagrangian Sensor Particles (LSPs) are engineered by the Helmholtz-Zentrum Dresden-Rossendorf in Germany (HZDR) (Fig. 2) [29]. They are composed of two half shells (Polyamid P4000, chemically polished), which are connected with a threaded rod and sealed with an o-ring. With a diameter of $d_{LSP} = 40.0 \cdot 10^{-3}$ m their weight is approximately $m_{LSP} = 33.0 \cdot 10^{-3}$ kg including all internal electronics (microcontroller, pressure sensor, battery, etc.). Similarly to previous experiments [32], the current investigation exclusively evaluates pressure sensor data collected at a frequency of approximately 50 Hz, which are stored on an SD card onboard during the experiments and retrieved subsequently. The 24 bit stainless steel piezoresistive pressure sensor 89BSD (TE Connectivity) offers a measurement range of 0 to 6 bar with a pressure resolution $p_{res} = 9$ Pa (corresponds to approximately 0.9 mm in height) at an oversampling ratio of 4096 samples [49]. For each impeller frequency, at least 14 single LSP trials are analyzed. The corresponding particle volume fraction is $\Phi_{LSP,exp} \leq 0.8 \cdot 10^{-5}$. The recording time of a single LSP in one trial is $t_{rec,single,exp} \leq 1$ h, totaling a measurement duration of 13.0 h for each dataset (see Gitlab project). The experimental data for each LSP run is preprocessed with a low-pass moving average filter of 15 consecutive values and, for comparability, interpolated with the *spline* method to a uniform 50.0 Hz signal, since the original sampling rates vary between 49.8 Hz and 50.0 Hz.

The LSP density calibration method, recently published in Hofmann et al. [32], is conducted identically in this study. Two glass vessels are prepared: the first contains the medium of interest from inside the STR, accessible through the bottom valve V-1/4 (Fig. 1), and the second is a sodium chloride (NaCL) solution adjusted to the upper allowed density limit (Table 1). By turning the upper half-shell of the LSP to modify the volume, and thus the density, it is adjusted to slowly sink in the first vessel and slowly rise in the second. The temperature of both vessels is kept constant with a water bath at the reactor temperature T.

Table 2
Overview of volumetric power inputs PV^{-1}, stirrer Reynolds numbers Re_{STR}, tip speeds u_{tip}, root mean square of the fluid velocity fluctuations from simulations $u_{rms,sim}$, estimated Taylor scales L_E based on the latter, Kolmogorov length scales λ_K and estimated minimum Kolmogorov length scales in the vicinity of the impeller tip $\lambda_{K,\phi=115}$.

Mixing parameter	Impeller frequency n / rpm			
	32	40	55	63
PV^{-1} / W m^{-3}	10.2	20.0	52.0	78.1
Re_{STR} $(\cdot 10^5)$ / –	2.5	3.1	4.3	4.9
u_{tip} / m s^{-1}	1.1	1.4	1.9	2.2
$u'_{rms,sim}$ $(\cdot 10^{-1})$ / m s^{-1}	1.2	1.5	1.9	2.3
$L_E(u'_{rms,sim})$ $(\cdot 10^{-3})$ / m	4.6	3.9	3.2	3.1
λ_K $(\cdot 10^{-6})$ / m	95.7	81.0	63.8	57.6
$\lambda_{K,\phi=115}$ $(\cdot 10^{-6})$ / m	29.3	24.7	19.5	17.6

2.3. Stokes number estimations and calculations

In process engineering and specifically in fluid mechanics, dimensionless numbers facilitate the comprehension, characterization, and prediction of an investigated system across varying scales. In numerous publications, the Stokes number St is defined as the ratio of the particle relaxation time to the characteristic flow time scale [50]

$$St = \frac{\tau_p}{\tau_f}, \tag{7}$$

and is used to quantify the flow-following capability of particles within a fluid [51]. In the context of single-point flow statistics in turbulent particle-laden flows, Ouellette et al. suggest that particles are effective flow tracers, if the Stokes number is in the order of magnitude of $St \approx \mathcal{O}(10^{-2})$ [52]. Tropea et al. mention a sufficient level of accuracy in flow tracing when $St < 0.1$, with errors remaining below 1% [53]. In previous studies, it has been shown that the Stokes number applies as a reference point for the classification of LSPs in STRs, even for LSP sizes as used in this study, which is $d_{LSP} \, \lambda_K^{-1} \approx \mathcal{O}(10^3)$ [27,32].

Generally, the particle relaxation time

$$\tau_p = \frac{4}{3} \frac{\rho_p \, d_p^2}{\eta \, c_D \, Re_p}, \tag{8}$$

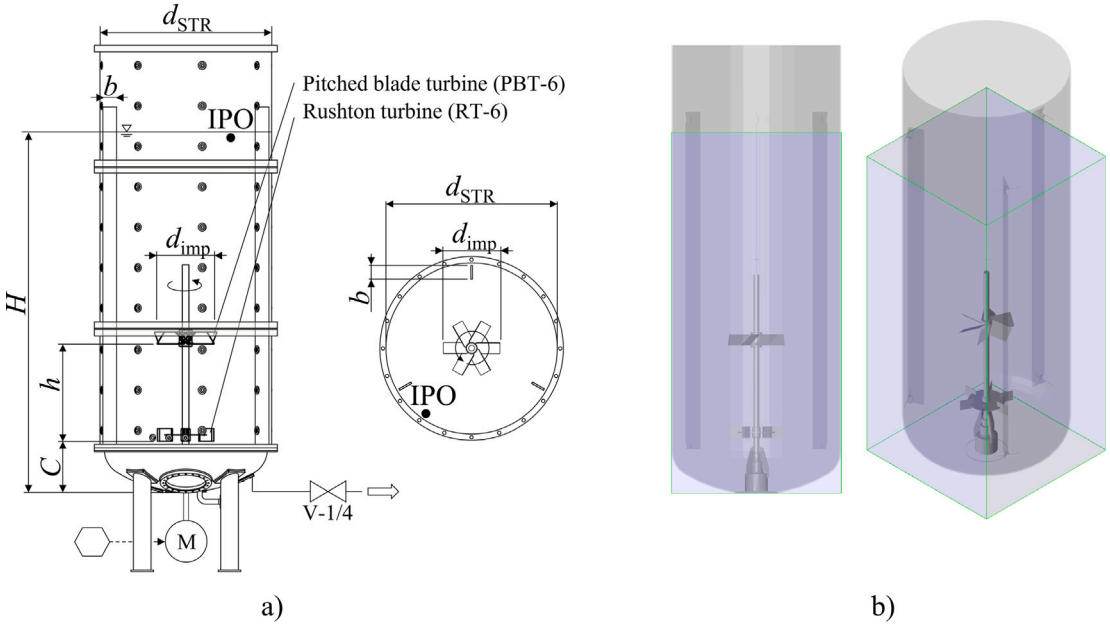

Fig. 1. (a) Schematic depiction of the acrylic glass reactor with a filling level of H, and a diameter of d_{STR}, equipped with three baffles of a width b. A Rushton turbine (RT-6, first stage) and a pitched blade turbine (PBT-6, second stage) with a diameter of d_{imp} are installed with a spacing of h and an off-bottom clearance of C. Fluid samples are taken from valve V-1/4. The location of the injection point (IPO) for hydrochloric acid and sodium chloride for the mixing time experiments is indicated with a black dot in the side view and the top view. (b) Schematic views of the STR with a green bounding box indicating the main lattice domain for the numerical simulations. (For interpretation of the references to color in this figure legend, the reader is referred to the web version of this article.)

Fig. 2. Depiction of the LSP design by Buntkiel et al. [29] with the two connected half-shells (left), the top half-shell with its threaded rod (center), and the bottom half-shell including the electronics (right) [33].

with the particle density ρ_p, the particle diameter d_p, the dynamic viscosity η, the drag coefficient c_D according to Haider and Levenspiel [54], and the particle Reynolds number Re_p originates from the simplified version of the equation of motion in stationary flows [55]. This approach considers non-Stokesian drag, which plays a dominant role in the herein investigated Re_p due to the wake generated behind the particle [56]. In case of inertial particles, the particle Reynolds number

$$Re_p = \frac{\rho_f \, d_p \, |u - v|}{\eta}, \tag{9}$$

needs to be solved and contains the fluid density ρ_f and the slip velocity $|u - v|$, which are the relative velocities between the undisturbed fluid flow u and the LSP v.

The characteristic large eddy turnover time of the surrounding fluid

$$\tau_f = \frac{L}{u}, \tag{10}$$

with L being the characteristic fluid flow length scale of the undisturbed flow and u being the undisturbed carrier fluid velocity is challenging to determine experimentally on an industrial scale.

However, in terms of L, three approaches are presented in previous studies: it can be chosen as (i) the Taylor scale L_E (Eq. (11)) [32], (ii) the macro-scale of the turbulence, which is approximately the size of the impeller diameter d_{imp} (Eq. (12)) [57], or (iii) a compromise between the turbulence length scale Λ (or the integral length scale) according to Ochieng et al. with $\Lambda = 0.1\, d_{imp} = 0.067\,\text{m}$ [58] and the particle size ($d_p = 0.040\,\text{m}$) on the one hand, and the Taylor scale $L_E(u'_{rms,sim})$ and the distance between the lattice points in the numerical simulation ($\Delta x = 0.004\,\text{m}$) [34] on the other hand. A characteristic flow length scale of the mean flow $L_{MF} = 20 \cdot 10^{-3}\,\text{m}$ is chosen to represent a good compromise between the mentioned scales and being just within the inertial subrange on the one hand and a high resolution on the other (Eq. (17)).

With regard to velocity, especially slip velocity, two approaches can be chosen: (i) using the simplified method, which takes the difference of the tip velocity u_{tip} and the maximum average axial velocity from the experiments into account as $u_{tip} - |\overline{v}|_{z,max}$, or (ii) using the velocity vectors from the LB LES.

In terms of the first approach, considering experimental results, this concludes to three simplified temporal scales

$$\tau_{f,micro-scale} = \frac{L_E}{u_{tip}} \text{ [32]}, \tag{11}$$

$$\tau_{f,meso-scale} = \frac{d_{imp}}{u_{tip}} \text{ [28]}, \tag{12}$$

and

$$\tau_{f,macro-scale} = \bar{t}_{circ,overall} \text{ [28]}, \tag{13}$$

where the latter accounts for the macroscopic effects and utilizes the overall average circulation time $\bar{t}_{circ,overall}$ of LSPs in an STR, similarly to the understanding of the global mixing time [59,60]. With the knowledge that the root mean square of the fluid velocity fluctuations is approximately $0.1 \cdot u_{tip}$ in this STR, Eq. (6) and (11) are further derived to

$$\tau_{f,micro-scale} = 0.1 \cdot \sqrt{\frac{15\,\nu}{\bar{\varepsilon}_T}}. \tag{14}$$

The second approach takes only numerical simulation results into account in order to solve Eqs. (9) and (10). To do so, Bellani et al.

present one approach with a stochastic slip velocity of large neutrally buoyant particles [61]. They suggest

$$\boldsymbol{V}_{\mathrm{slip,stoch}} = \sqrt{\overline{\boldsymbol{u}'^2} - \overline{\boldsymbol{v}'^2}}, \tag{15}$$

where the primes account for the velocity fluctuation relative to the average value, e.g. for the radial fluid velocity component $u'_{\mathrm{r},i} = u_{\mathrm{r},i} - \overline{u_{\mathrm{r}}}$. Hence, the stochastic fluid velocity fluctuation magnitude of the tracer is defined as

$$\boldsymbol{u}_{\mathrm{stoch}} = \sqrt{\overline{\boldsymbol{u}'^2}}, \tag{16}$$

which is also presented in this study for comparison.

In order to obtain spatially resolved Stokes numbers for the mean flow (MF) [48] throughout the reactor, the numerical simulations presented herein provide 3-dimensional information about the velocities $\boldsymbol{u}$ of the fluid and $\boldsymbol{v}$ of the LSPs. Therefore, the euclidean norm $\|\cdot\|$ of the slip velocity vector and the fluid velocity vector is considered, along with the characteristic length scale of the mean flow L_{MF}, which results in

$$St_{\mathrm{MF}} = \frac{4}{3}\frac{\rho_{\mathrm{p}}}{\rho_{\mathrm{f}}}\frac{d_{\mathrm{p}}}{\|\boldsymbol{u}-\boldsymbol{v}\|_2\, c_{\mathrm{D}}}\frac{\|\boldsymbol{u}\|_2}{L_{\mathrm{MF}}}, \tag{17}$$

and is similarly used in a previous study on laboratory scale with inertial, finite-sized particles in a 4D-Particle Tracking Velocimetry (4D-PTV) setup with accompanying numerical simulations [34].

2.4. Lattice-Boltzmann simulations

The numerical simulations are conducted with M-Star CFD (M-Star Simulations, LLC, Version 3.10.32), which utilizes a Boltzmann solver to essentially numerically solve the Navier Stokes equation through the use of the Boltzmann transport equation as

$$\frac{\partial f}{\partial t} + \boldsymbol{\zeta}^T \nabla_x f + \boldsymbol{F}_{\mathrm{ext}}^T \nabla_\zeta f = \Omega(f) \text{ [8,38,62,63].} \tag{18}$$

The equation is spatiotemporally discretized for a D3Q19 set of lattice points (Fig. 3). The Boltzmann equation consists of f, which is the time derivative of the particle distribution, $\boldsymbol{\zeta}$ as the velocity and $\boldsymbol{F}_{\mathrm{ext}}$ as the external forces of the D3Q19 model. The right side of the equation includes Ω(f), the collision parameter, for which the Bhatnagar–Gross–Krook parameter

$$\Omega(f) = -\frac{1}{\tau_{\mathrm{c}}} \cdot \left(f - f^{\mathrm{eq}}\right) \tag{19}$$

is used [62,64–66]. It is in the collision parameter where the collision time τ_{c} and f^{eq} are included. The variable quantifies the time between particle collisions and the equilibrium particle distribution, respectively. This allows for the solution of the Boltzmann equation

$$f_i(\boldsymbol{x} + \boldsymbol{c}_i \Delta t, t + \Delta t) = f_i(\boldsymbol{x}, t) + \Delta t\, \Omega_i(\boldsymbol{x}, t) \text{ [8,62,64–66].} \tag{20}$$

The bounding box with green edges in Fig. 1 (b) highlights the main lattice domain of the STR, while the blue shade within the box denotes the respective filling height H to achieve the $V = 12.5\,\mathrm{m}^3$ filling volume. To guarantee the validity of the study, an extensive grid independence study is conducted. The results are given in Appendix A. A mesh with 500 lattice points (LX 500) across the horizontal diameter and 1062 lattice points along the vertical axis of the STR is found to be the ideal trade-off between accurately calculating small eddies, not receiving physically unlikely results, and calculation capacity of the respective cluster hardware. The total number of lattice sites is equivalent to around 265.5 million across the main lattice domain. The lattice spacing, particularly the spacing across the impeller diameter, is consistent with the recommended number of lattice sites for a Rushton turbine and a PBT-6 configuration, guaranteeing grid independence [42]. Furthermore, the preliminary grid independency study coincides with the results proclaimed by Šrom et al. who worked with the same STR but applied refinement zones for areas of higher

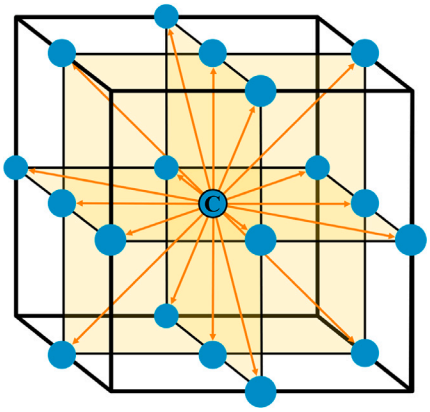

Fig. 3. Discrete velocity vectors pointing from the center lattice point (C) to all nearest neighbors in a D3Q19 Lattice-Boltzmann model structure.

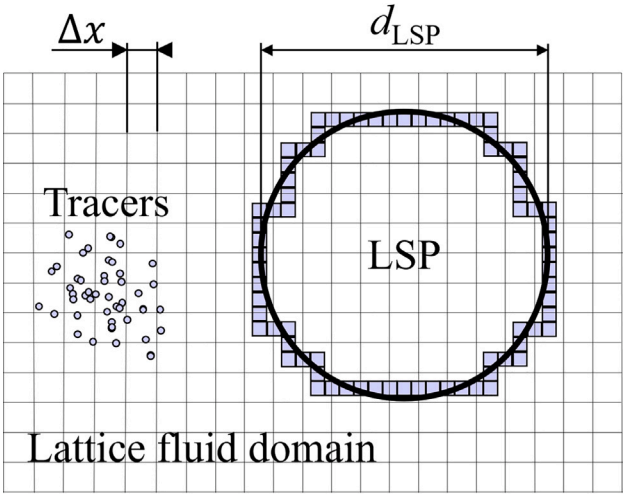

Fig. 4. Exemplary 2-dimensional depiction of the lattice domain with a lattice spacing of Δx, showing the two types of simulated particles used in this study: non-inertial, non-interacting point objects referred to as flow tracers (*tracer,sim*, left), and an LSP (*LSP,sim*, right) treated as a discrete element particle (thick circle demonstrates a set of Lagrangian points). For the latter and as a reference, the coarse computational boundary (squares) based on bounce-back rules of the LB method is shown according to Feng and Michaelides, but not used in this study [41].

turbulence [13]. The application of such refinements is not applied in the present study, as for the use of resolved particles nested in the application of the immersed boundary method, a constant set of contact points with the lattice structure provided more stable results. Additionally, the resolution in this study surpasses the recommended refinement required for a minimum resolution of 80% of the kinetic energy in the bulk of the STR [13,67].

For the study, a Courant number of $Co = 0.02$ was set with the fluid surface set to single phase under free slip conditions. The remaining system boundaries are set to no slip. The large eddy simulation model (LES) is applied as a turbulence model with a Smargorinsky coefficient of $C_{\mathrm{s}} = 0.1$.

The simulated time for each operating point is a total of 515 s, with the first 35 s being disregarded because the STR is still reaching steady state during this period of time. Statistics and output files are saved with a frequency of 50 Hz once steady state is reached, which is a total simulated time of $t_{\mathrm{sim,max}} = 480\,\mathrm{s}$.

The particles simulated in the study are simulated as spheres (*LSP,sim*), set to the same diameter ($d_{\mathrm{p}} = 0.04\,\mathrm{m}$), replicating the LSPs used by Buntkiel et al. and Hofmann et al. [29,32]. The density of the

particles is set at $\rho_p = 999.8\,\mathrm{kg\,m^{-3}}$, to match the work of Buntkiel et al. The idea behind the resolved particles is that with sufficient coverage of the particle surface through various lattice points, the physical characteristics of the particle can be deduced from the solver itself, through the immersed boundary Lattice-Boltzmann method [41]. In the current case, the lattice spacing of 0.004 m guarantees that each LSP has approximately ten lattice sites over its diameter d_{LSP} (Fig. 4). From steady state on, output statistics for resolved particles are saved every 0.02 s. The initial release of the particles takes one second into the simulation, allowing for an even distribution starting point for the output statistics after steady-state is attained. A total of 98 LSPs mimicking resolved particles are simulated, amounting to a total of 13.0 h in data obtained from a Lagrangian perspective per rpm case, matching the amount of recorded lifeline data from the experimental work. The solid–particle interaction is set to bounce, allowing the particles to come in contact with the impellers; the particle–particle interaction is set to Hertz simple, following the standard settings of M-Star for a nonelastic collision of particles [42].

The preliminary simulations pertaining to the grid independence were conducted on a local cluster consisting of two AMD Epyc 7702 64 core processors and two NVIDIA Tesla A100 with 40 GB memory each. The further resolved particles and lifeline simulations were conducted on the high-performance computing cluster of the Hamburg University of Technology, using two AMD Epyc 9124 and two NVIDIA Tesla H100 GPUs, with wall clock times ranging from 5 to 7 days depending on the simulated operating point.

Before being used in the evaluation algorithm, the simulated data are checked in three steps to ensure meaningfulness and comparability with the experimental data in the identical geometrical vessel. First, any dataset in which 50 data points in total (corresponding to 1 s physical time) have values higher than the experimental filling level or lower than the lowest point in the reactor is discarded. Second, any dataset in which 250 consecutive data points (corresponding to 5 s physical time) have an axial distance of 0.04 m to the filling level are treated as *floating*, and thus are discarded. Third, any dataset whose correlation matrix has a pairwise linear correlation coefficient $\gamma > 0.98$ and a respective p-value < 0.02 is also discarded, as this indicates identical datasets. The remaining datasets of each rpm case are reduced to a duration of $t_{rec,tot,sim} = 13.0$ h.

The simulations of the resolved particles (*LSP,sim*) that mimic the experimental LSPs (*LSP,exp*) are further accompanied by the addition of non-inertial, non-interacting point objects referred to as flow tracers (*tracer,sim*) providing a full Lagrangian representation of the undisturbed fluid field. The steps and criteria for using the data follow those for the resolved particles.

2.5. Utilization of the pressure sensor data and corresponding simulation data

In this study, data from three different particle types is evaluated: experimental data of LSPs (*LSP,exp*) is compared to the data of simulated LSPs (*LSP,sim*) and simulated undisturbed fluid flow tracers (*tracer,sim*) in the same reactor setup. To do so, the time-dependent axial position

$$z(t) = H - \frac{p(t) - p_0}{\rho_f\, g} \tag{21}$$

of an experimental LSP is determined by using the recorded hydrostatic pressure p, the ambient pressure p_0 before each trial for each LSP, the fluid density ρ_f (Table 1), and the gravitational acceleration g [29,32].

Deriving these Lagrangian data points by time, the Lagrangian axial velocity

$$v_z(t) = \frac{\mathrm{d}z(t)}{\mathrm{d}t} \tag{22}$$

is obtained. Furthermore, by subdividing the reactor into 42 vertical slices j, each with a height of $h_j = 0.1$ m, Eulerian data such as the probability of presence for each bin

$$P_j = \frac{N_j}{\sum_{j=1}^{42} N} \cdot 100\%, \tag{23}$$

where N_j are the counts in the respective bin j, as well as axial velocity distributions for $v_{z,neg}$ (negative, downward movement) and $v_{z,pos}$ (positive, upward movement) over the reactor height are derived. However, single-point Lagrangian axial velocity statistics are also presented in this study based on absolute velocities $|v|_j = v_{z,mag}$ and are depicted as probability density functions (PDF). The 3-dimensional location and velocity data from the numerical simulations are taken and evaluated directly with the same sampling rate as in the experiments.

For the hydrodynamic characterization of the STR, the circulation time distribution t_{circ} (CTD) over the reactor height and the hydraulic mean residence time distribution τ (RTD) over the reactor height are calculated for all three particle types. Both evaluations allow for the qualitative analysis of axial hydrodynamic compartments. Therefore, for the CTD, the time differences $t_{circ,j,dt}$ are calculated based on the duration it takes a particle to cross the central plane of slice j from top to bottom or from bottom to top, first at the initial time $t_{circ,j,t=0}$ and subsequently at $t_{circ,j,t>0}$ [28,32]. Regarding the RTD, the particle volume flow rates $\dot{V}_j$ in the respective reactor volumes V_j with their surface areas A_j are calculated according to

$$\left|\vec{\dot{V}}\right|_j = |\vec{v}|_j \cdot A_j, \tag{24}$$

eventually leading to the particle hydraulic residence time

$$\overline{\tau}_j = \frac{\dot{V}_j}{\left|\vec{\dot{V}}\right|_j}. \tag{25}$$

Due to partly different recording lengths of the trials or counts over the reactor height, a weighted average of the value x is determined as

$$\overline{x} = \frac{\sum_{i=1}^{M} w_i x_i}{\sum_{i=1}^{M} w_i}, \tag{26}$$

with the weight w of the respective trial i of total M trials per dataset. Corresponding uncertainties of the mean $\Delta_{\overline{x}}$ are based on the calculation of the standard deviation of the individual measurement from the mean Δ_x and, if applicable, an error propagation. For a detailed documentation of the calculations the reader is referred to the Gitlab repository.

An investigation of the dynamic pressure acting on the LSP and the resulting height error is discussed in [68] with similar designs. The experimental results presented herein in combination with the numerical simulations come to a similar conclusion that those are negligible. Even at the highest impeller frequency of $n = 63$ rpm ($u_{tip} = 2.2\,\mathrm{m\,s^{-1}}$), the estimate of the maximum dynamic pressure fluctuation at the tip of the impeller is approximately 128 Pa, which corresponds to a relatively low height tolerance of approximately 13 mm compared to the bin size $h_j = 100$ mm.

2.6. Particle volume fraction sensitivity study for numerical simulations

Due to the complexity of the resolved particle LB LES utilized herein and the associated demanding wall clock time, it is essential to obtain the maximum possible amount of data within the approximately 210 h available on the high-performance cluster. However, a numerical replica of the experimental trials with a perpetual physical time of 1.0 h per LSP with a maximum of three LSPs in the STR is not possible. This is the reason why 98 particles are eventually used, each with $t_{sim,max} = 480$ s physical time, totaling 13.0 h of data for each particle type, *LSP,sim* and *tracer,sim*. Those 98 LSPs are the result of the aforementioned elimination algorithm (Chap. 2.4), but initially there are approximately $N_{LSP,sim} = 250$ LSPs in the STR.

Multiple studies have extensively focused on characterizing turbulence attenuation in particle-laden flows [61,69–71]. Due to the large number of inertial, finite-sized, neutrally buoyant particles in the LB LES, a sensitivity study is carried out at 55 rpm, scrutinizing the decrease in turbulence of the carrier fluid, as well as particle perturbation and collision, as a function of five LSP quantities, $N_{\mathrm{LSP,sim}} \in \{18, 44, 92, 155, 304\}$, corresponding to volume fractions $\Phi_{\mathrm{LSP,sim}} \in \{0.5, 1.2, 2.5, 4.2, 8.1\} \cdot 10^{-4}$. For each case, and additionally for a run without LSPs, 660 tracers are submerged in the same run together with the different number of LSPs to record a potential turbulence attenuation of the fluid. Each particle type is recorded for a physical time of 60 s at a frequency of 50 Hz, totaling 11.0 h tracer data.

One approach is described by Crowe et al. [50], which helps to classify the dispersed phase flow in the STR as *dense* or *dilute*. If the ratio of the particle response time τ_{p} to the time between collisions τ_{c} is

$$\frac{\tau_{\mathrm{p}}}{\tau_{\mathrm{c}}} < 1, \tag{27}$$

the flow is considered as dilute, since the particles have sufficient time to adjust to local fluid dynamic forces. The time between the collisions is defined as

$$\tau_{\mathrm{c}} = \frac{1}{\frac{N_{\mathrm{LSP,sim}}}{V}\, \pi\, d_{\mathrm{p}}^2\, \boldsymbol{V}_{\mathrm{slip,stoch}}}. \tag{28}$$

The second approach examines the velocity fluctuations $\boldsymbol{u}'^2_{\mathrm{rms}}$ of all three velocity vector components (in cylindrical coordinates) as a function of the volume fractions according to Cisse et al. and Bellani et al. [72,73] in the form of

$$u'^2_{\mathrm{rms}} = \overline{(u_i - \overline{u_i})^2}, \tag{29}$$

with u_i being a single fluid velocity vector in time, and $\overline{u_i}$ representing the average over time. Moreover, the turbulent kinetic energy (TKE)

$$k = \frac{1}{2}(u'^2_{z,\mathrm{rms}} + u'^2_{r,\mathrm{rms}} + u'^2_{\theta,\mathrm{rms}}) \tag{30}$$

is used to potentially determine a decrease with an increasing particle number.

The third approach is presented by Ouellette et al. [70] and Hofmann et al. [34] as single point statistics via a probability density of all Lagrangian velocities occurring in comparison to the undisturbed fluid flow tracers.

2.7. Global mixing times and local mixing time distributions

Regarding the detailed description of the determination of the global mixing time, the reader is referred to the previous study [32]. The decoloration method with bromothymol blue (BTB) is conducted with the addition of a 2 M hydrochloric acid (HCl) and a 2 M sodium hydroxide (NaOH) solution during the LSP trials. The injection point of HCl (IPO) is located 13° behind the baffle in the impeller's rotational direction (Fig. 1). The injection lasts 23 s with the 250 mL HCl solution mixed with an aqueous 3 L sodium chloride (NaCL) solution of 312.5 g L^{-1} in deionized water (DW). The latter has no influence whatsoever on the trials described herein. Uniform lighting is provided by eight LED panels and a white diffuser fabric positioned behind the reactor. The decoloration is recorded at a frequency of 30 Hz using a NIKON D7500 camera with a SIGMA lens (1:1.8, 20 mm f22.0) at a resolution of 1920 × 1080 pixels. Post-processing and the evaluation of the mixing times is performed by an in-house developed MATLAB algorithm, which utilizes the trend of normalized gray scale values over time. By definition, the global mixing time criterion of 95% is achieved once the normalized sensor output reaches and remains between 0.95 and 1.05 of its final value [74]. In this study, each mixing time experiment is conducted in triplicates for the impeller frequencies $n \in \{24, 32, 40, 55, 63\}$ rpm. Hence, the normalized sensor output over time is the gray scale intensity I'_{t}, which is plotted as the log variance

$$\log\, \sigma_{\mathrm{I}}^2 = \log((I'_{\mathrm{t}} - 1)^2) \tag{31}$$

over time.

However, in order to determine heterogeneities in the form of compartments, it is insufficient to evaluate the entire reactor as a single entity and obtain only the global mixing time $\Theta_{\mathrm{glob,95}}$. Therefore, as shown in a previous study [59], for a 2 × 2 pixel array throughout selected gray scale images over time, a respective mixing time is calculated, which yields the local mixing time $\Theta_{\mathrm{loc,95}}$. For this purpose, a *moving average* filter is used to calculate the smoothed gray values. Eventually, the relative local mixing time is plotted as a ratio of

$$\Theta^* = \frac{\Theta_{\mathrm{loc,95}}}{\Theta_{\mathrm{glob,95}}}. \tag{32}$$

3. Results and discussion

3.1. Numerical simulation sensitivity study

The sensitivity study focuses exclusively on the Lattice-Boltzmann large eddy simulations (LB LES) data with different numbers of Lagrangian Sensor Particles (LSPs) in the stirred tank reactor (STR), and examines the influence of large, nearly neutrally buoyant particles with a diameter of $d_{\mathrm{LSP}} = 40$ mm on the intensity of turbulence fluctuations. This necessitates a dilute flow so that disturbances in the carrier fluid remain isolated without interference [72]. According to Crowe et al. [50], all particle volume fractions examined in this study meet the criterion that the ratio of the particle response time to particle collision time $\tau_{\mathrm{p}}\, \tau_{\mathrm{c}}^{-1} < 1$, being far below 0.1 (Table 7 in Appendix B). These estimations use the stochastic slip velocity $\boldsymbol{V}_{\mathrm{slip,stoch}} \approx 0.135$ m s^{-1} and the calculated values for $\tau_{\mathrm{p}} \approx 1.0$ s, such as the drag coefficient $c_{\mathrm{D}} \approx 0.4$ and the particle Reynolds number $Re_{\mathrm{p}} \approx 5.7 \cdot 10^3$. Nevertheless, direct particle interactions are observed through collisions or perturbations within a distance of their respective boundary layer of d_{p} [75] by calculating the probability of particle collision or perturbation (PCP). The results demonstrate a PCP between 3.75% and 7.33% for the particle number used in the main study (Fig. 5).

Highlighting the fluid velocity fluctuation variance u^2_{rms}, which shows the instantaneous fluctuation from the mean, a decrease can be observed for the three velocity components with an increasing particle volume fraction $\Phi_{\mathrm{LSP,sim}}$ (Fig. 5). Literature findings confirm this behavior, as well as a proposed fitting to $(1 - (3.75 \cdot \Phi^{2/3}_{\mathrm{LSP,sim}}))$ (gray dashed trends), despite the use of higher particle number densities [72]. Moreover, a decrease of the turbulent kinetic energy (TKE) k of approx. 10% between the lowest and highest volume fraction is shown, which also pertains to the findings of Bellani et al. albeit for a lower particle Reynolds numbers $Re_{\mathrm{p}} = 175$ and $\Phi_{\mathrm{LSP,sim}} = 1.4 \cdot 10^{-3}$ relative to single phase [73]. The single-point velocity statistics of the fluid appear not to be affected by the presence of LSPs (Fig. 18 in Appendix B).

These findings indicate that at the particle volume fraction used in the main study, the LSPs already substantially perceive the presence of neighboring particles through alterations in the flow and through collisions that occur. On a small scale, no significant turbulence disturbance can be observed, whereas a slight attenuation is seen globally. This entails in a general decrease in the velocity of the simulated LSPs because of the substantial volume fraction. This impact is specific to the simulations, as the experiments utilize significantly lower volume fractions.

3.2. Axial velocity distributions

The first visualization presents information about the velocity of all three particle types (experimental LSPs, simulated LSPs and tracers). To do so, the derivative of the height position over time $\mathrm{d}z(t)\,\mathrm{d}t^{-1}$ yields the axial velocity $v_z(t)$ along the trajectory of the particle. Binning the datasets of the three particle types over the reactor height in 42 slices j provides information of the average axial velocity distribution for both

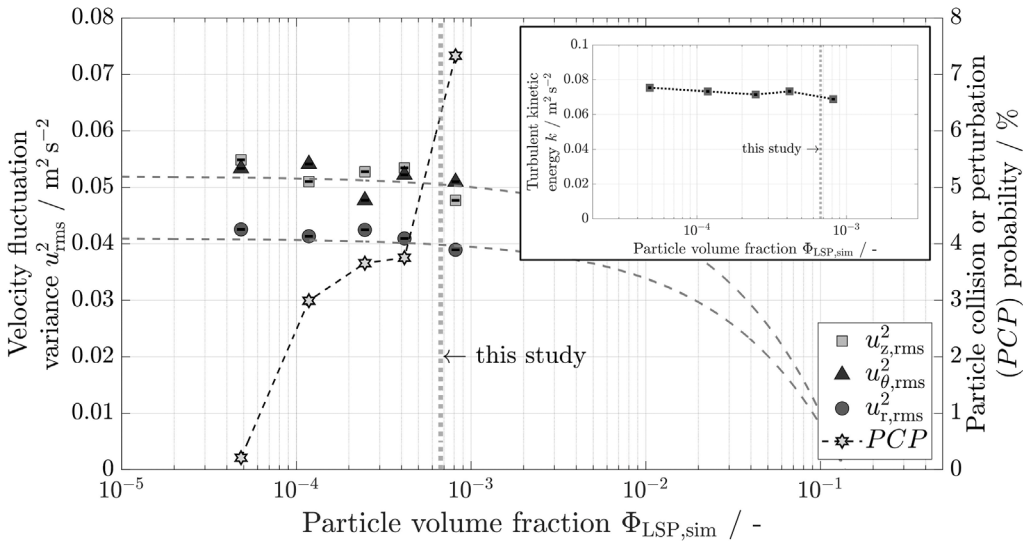

Fig. 5. Left y-axis: Velocity fluctuation variances for the three cylinder coordinate components $u^2_{z,rms}$ (squares), $u^2_{r,rms}$ (triangles), and $u^2_{\theta,rms}$ (circles) as a function of different particle volume fractions $\Phi_{LSP,sim}$ for $n = 55$ rpm. The dashed lines are a fit to $(1 - (3.75 \cdot \Phi^{2/3}_{LSP,sim}))$. Right y-axis: Particle collision or perturbation PCP probability (hexagram) within a distance of a boundary layer of d_p. Inset: Turbulent kinetic energy (TKE) k as a function of $\Phi_{LSP,sim}$ for $n = 55$ rpm. Vertical dashed lines represent the volume fraction used in the main study.

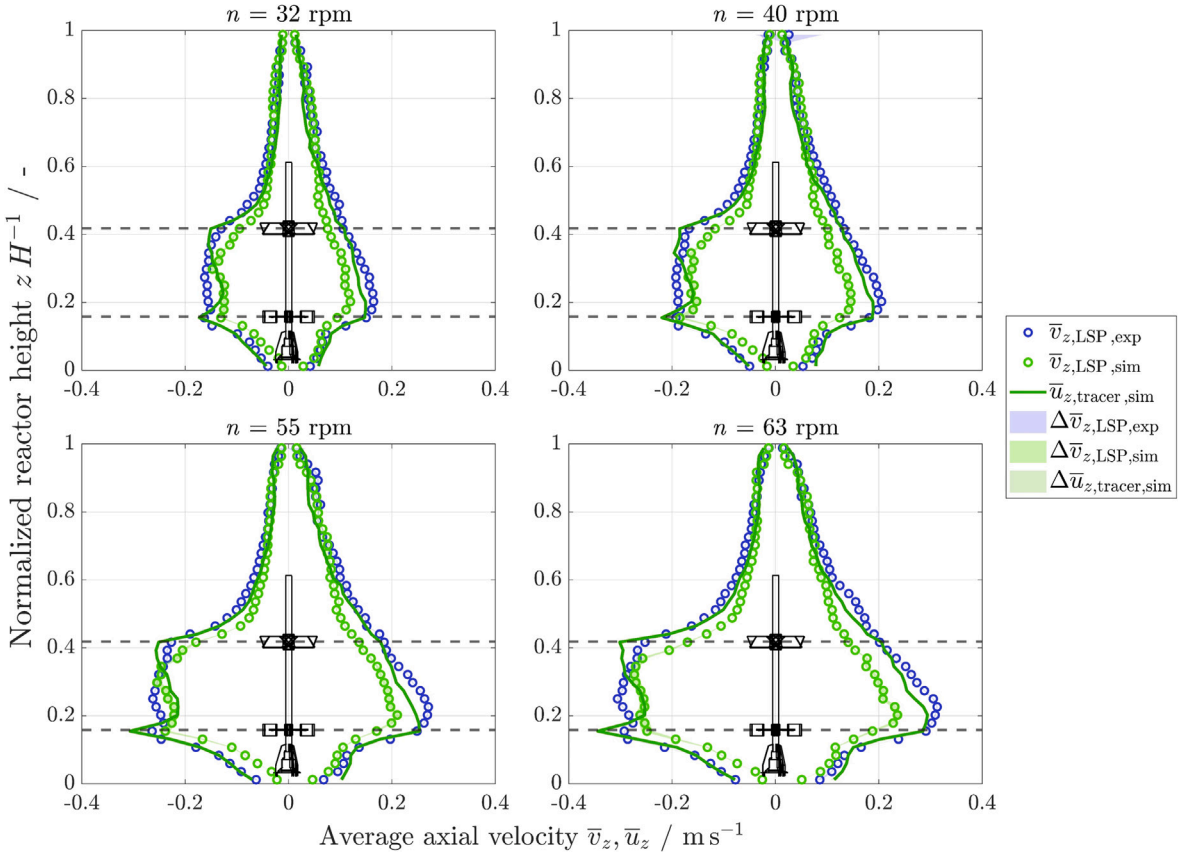

Fig. 6. Average positive (upwards flow) and negative (downwards flow) axial LSP velocity $\overline{v}_z$ and tracer velocity $\overline{u}_z$ distributions as a function of the normalized reactor height z (H = 4.2 m) for experimental LSPs (*LSP,exp*, blue circles), simulated LSPs (*LSP,sim*, green circles), and for simulated tracer (*tracer,sim*, green line), each for the rpm cases $n \in \{32, 40, 55, 63\}$ rpm. The vertical bin size is 10 cm. The shaded areas depict the uncertainty Δ of the respective dataset. The gray dashed lines indicate the center position of the RT-6 (lower) and PBT-6 (upper). (For interpretation of the references to color in this figure legend, the reader is referred to the web version of this article.)

negative (downward movement) and positive (upward movement) velocities $\overline{u}_z$ and $\overline{v}_z$ of the tracers and the LSPs, respectively. Fig. 6 reveals the characteristic profiles of the four rpm cases $n \in \{32, 40, 50, 63\}$ rpm.

Generally, all trends show the highest average axial velocities at the height of the impellers (gray dashed lines), and with increasing distance from them, the velocity decreases. The undisturbed tracer particles (green line) have a sharp peak at both impeller positions in the downward direction, whereas upwards a more rounded peak becomes apparent at the RT-6. Above the latter ($z\,H^{-1} \approx 0.25$), a distinguished suction zone toward RT-6 is recognizable by a sudden velocity decrease

in the downward direction. At first glance, the experimental LSPs (blue dots) seem to have the overall highest average axial velocity. However, between the RT-6 and the reactor bottom and in the aforementioned peak zones at both impellers, their average axial velocity is less than that of the tracers. The higher the impeller frequency, the more distinct the negative velocity drop in the suction zone above the RT-6. The simulated LSPs (green dots) show a trend similar to the experimental ones, especially in the upper third of the reactor. Nevertheless, the maximum average axial velocity difference between the simulated and experimental LSPs amounts to $\approx \{0.05, 0.06, 0.08, 0.10\}\,\mathrm{m\,s^{-1}}$ for all impeller frequencies, respectively, in terms of positive average axial velocities at the height of $z\,H^{-1} \approx 0.21$.

The prominent velocity difference between experimental and simulated LSPs is most likely due to the number of simulated LSPs in the reactor, whose effect on velocity is explained in the sensitivity study (Chap. 3.1). Another reason is found in the next Section 3.3, where the effects of a different center of mass on the LSP's velocity is elucidated. Although the utilized *LSP,exp* only have a mass offset of $r_{\mathrm{shift}} = 1.15\,\mathrm{mm}$ toward their geometrical center, they seem to break out easier of the upper less turbulent zone and thus show a faster vertical movement in combination with a higher probability in the zone between the impellers. The *LSP,sim* are more likely to be slowed down in the axial direction due to an easier facilitation of a horizontal velocity transition. The decrease in TKE of the fluid between 3% and 10% compared to the experimental runs, and additionally, the *PCP* probability between 3% and 7% add up to the difference shown in the axial velocity.

Another possibility of depicting axial velocities is presented in Fig. 7 for $n = 55\,\mathrm{rpm}$. This statistical evaluation in the form of a probability density function (PDF) uses all the Lagrangian velocities of the tracers $u_{z,\mathrm{mag}}$, and the LSPs $v_{z,\mathrm{mag}}$, as absolute values, and can be used for an unbiased plausibility confirmation of the obtained data. The upper depiction shows the obtained velocities in the entire reactor, whereas the center and lower depiction show the velocities in the high turbulent zones, at the height of the RT-6 and the PBT-6, respectively. The probabilities for the last two are normalized due to a different number of data points. The tip speed v_{tip} is marked with a vertical dashed line. Because the axial distribution of the tracers throughout the reactor is sufficiently homogeneous, it is used as a reference for this evaluation. Basically, the tracers show a higher probability at velocities of $0.9\,\mathrm{m\,s^{-1}}$ and above (upper and lower), or even of $0.75\,\mathrm{m\,s^{-1}}$ and above (center) than those of *LSP,exp* and *LSP,sim*, which is obvious, since they represent the undisturbed fluid. The highest velocities for both LSP types occur at the height of RT-6 (center) and PBT-6 (lower) with an overlapping trend starting at $0.8\,\mathrm{m\,s^{-1}}$, demonstrating their strong, but similar inertial behavior compared to the tracers in high turbulent zones. In those zones, the trends for slow velocities are also in good agreement, most likely representing the upward movement at the reactor walls or near the baffles. However, for *LSP,sim*, there is a clear probability gap around $\approx 0.5\,\mathrm{m\,s^{-1}}$, which is mainly due to their 3-fold lower probability of presence in the impeller zones compared to *LSP,exp*. Instead, *LSP,sim* show good agreement with the tracers at very low velocities up to $0.1\,\mathrm{m\,s^{-1}}$, due to their similar probability of presence in the upper half of the STR at low velocities. In total, *LSP,sim* have an approximate 78% probability of staying in such a low turbulent zone, compared to 40% for *LSP,exp*, which confirms the conclusion of the work of Rautenbach et al. [33] once again.

3.3. Vertical probabilities of presence

Moreover, for all three particle types (experimental LSPs, simulated LSPs and tracers), the height distribution during the trials is investigated. This information is pivotal, as all results, especially direct comparisons, are based on the location and the time each particle spent there.

Fig. 8 depicts the probabilities of presence over the normalized reactor height for the four rpm cases $n \in \{32, 40, 55, 63\}\,\mathrm{rpm}$. The

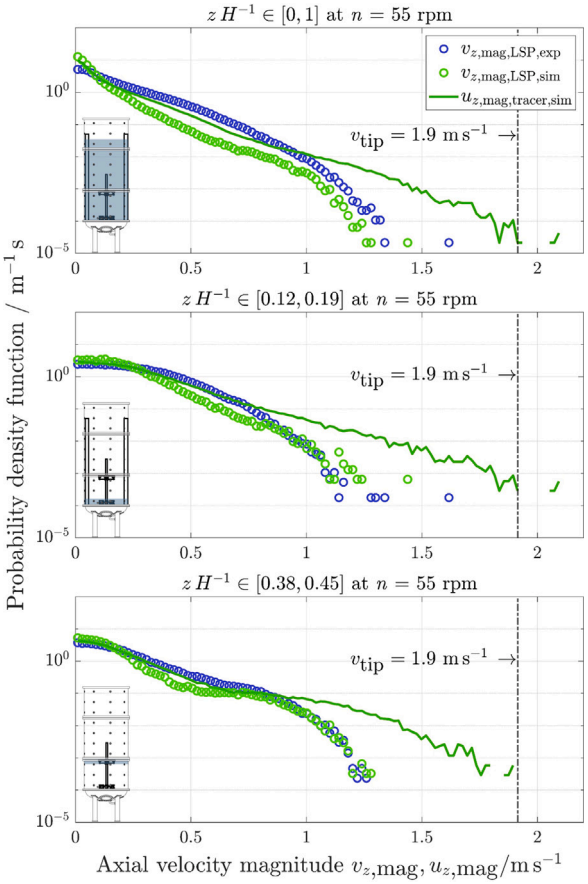

Fig. 7. Probability density function of Lagrangian axial LSP velocity magnitudes $v_{z,\mathrm{mag}}$ (experimental: blue circles; simulated: green dots) and tracer velocity magnitudes $u_{z,\mathrm{mag}}$ (green line) at $n = 55\,\mathrm{rpm}$. Upper: all axial velocities; Center: axial velocities at the height of the RT-6 (respectively normalized); Lower: axial velocities at the height of the PBT-6 (respectively normalized). (For interpretation of the references to color in this figure legend, the reader is referred to the web version of this article.)

undisturbed tracer particles (*tracer,sim*, green line) are nearly homogeneously distributed over the height. Generally, with an increasing impeller frequency their distribution trend gets more even throughout the reactor height. The characteristic behavior at the bottom is due to the dished shape of the reactor. Although experimental LSPs (*LSP,exp*, blue dots) seem to accumulate in the bottom of the reactor at 32 rpm, at higher frequencies, they tend to distribute well up to the pitched blade turbine (PBT-6, top dashed line). Above that impeller, the distribution drops to zero toward the top of the STR for all rpm cases. The simulated LSPs (*LSP,sim*, green dots) demonstrate the opposite behavior. Their distribution between the impellers is much lower than those of the experimental LSPs, almost mirrored at the tracer distribution trend. They show an even stronger accumulation at the very bottom of the reactor below the normalized height of $z\,H^{-1} \approx 0.1$ for all impeller frequencies, but a similar distribution as the tracers above the PBT-6. At the very top of the reactor they as well reveal a clustering behavior.

Even though the overall $2.34 \cdot 10^6$ gained data points for each rpm case are almost tripled compared to the previous study [32], the impeller setup used herein reveals a large, less turbulent zone in the upper half of the STR, which is clearly seen by the uneven trend of the tracers. This characteristic would necessitate an even larger dataset, in particular if mass transfer or heat transfer phenomena need to be examined in detail in the entirety of the STR for low impeller frequencies. For our study, the tracer data is sufficient with a low uncertainty and serves as a point of reference when analyzing LSP data. For 40 rpm and above, the *LSP,exp* trend at the Rushton turbine

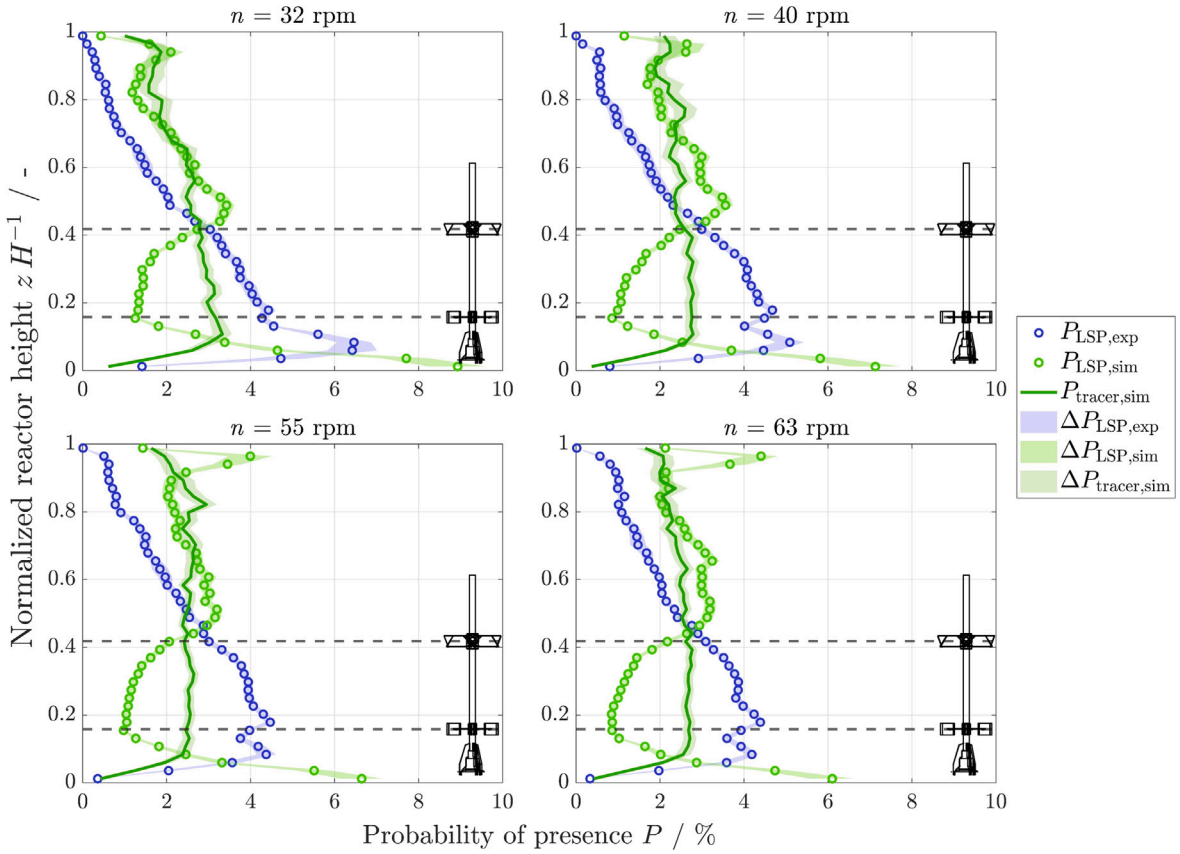

Fig. 8. Axial probability of presence P as a function of the normalized reactor height $z\,H^{-1}$ ($H = 4.2\,\mathrm{m}$) for experimental LSPs (*LSP,exp*, blue circles), simulated LSPs (*LSP,sim*, green circles), and for simulated tracer (*tracer,sim*, green line), each for the rpm cases $n \in \{32, 40, 55, 63\}\,\mathrm{rpm}$. The vertical bin size is 10 cm. The shaded areas depict the uncertainty Δ of the respective dataset. The gray dashed lines indicate the center position of the RT-6 (lower) and PBT-6 (upper). (For interpretation of the references to color in this figure legend, the reader is referred to the web version of this article.)

(RT-6, lower dashed line) is similar to a study published by Bisgaard et al. [76], with a sudden increase just above and below the impeller, which is explained by the formation of trailing vortices behind the impeller blades [77]. The general decline in the probability of presence toward the top is explained by the less turbulent zone in the upper half of the STR and the small but perceptible buoyancy difference of $(\rho_f + 1.0)\,\mathrm{kg\,m^{-3}}$. The density difference of the simulated LSPs is set slightly higher at $(\rho_f + 1.7)\,\mathrm{kg\,m^{-3}}$, since initial numerical attempts failed due to a large number of floating LSPs. This behavior was not observed in experiments. Interestingly, in terms of density differences, Lauterbach et al. found similar results in their CFD analysis. Using a Poincaré map, they demonstrated the best homogeneous distribution with an even higher particle density $(\rho_f + 50)\,\mathrm{kg\,m^{-3}} \leq \rho_p \leq (\rho_f + 100)\,\mathrm{kg\,m^{-3}}$ in a 2 L bioreactor [78]. However, their setup barely resembles the parameters used in this study. Hence, the balanced density difference used herein is chosen to minimize floating particles and reduce bottom accumulation in the reactor. As reported in the literature for particle-laden flows, most likely the particles already tend to cluster and collide in those regions with a prevailing characteristic Stokes number [79,80].

The characteristic behavior of the probability of presence of the *LSP,sim* can be explained by the results of a study by Rautenbach et al. [33]. Therein, the particle dynamics of two types of Lagrangian Particles (LP) of the same size ($d_p = 40\,\mathrm{mm}$) and density are experimentally investigated in a flow passage at similar fluid flow speeds. In one LP, the center of mass is offset by $r_{shift} = 6.50\,\mathrm{mm}$. In the second LP, the center of mass is located at the equatorial geometric center. Basically, those two LP types correspond to the two LSP types used in this study (experimental and numerical), since for *LSP,exp* the center of mass is offset by $r_{shift} = 1.15\,\mathrm{mm}$ due to the arrangement of the internal hardware components [29], and *LSP,sim* are spheres with their center of mass at their geometric center. The three principal conclusions of their work are directly transferable to this study:

1. Particles with a centrally situated center of mass, like the *LSP,sim*, show a more homogeneous probability of presence with a higher presence in the less turbulent region.
2. To perform horizontal flow direction changes, particles with an offset center of mass, such as *LSP,exp*, require stronger momentum. Hence, they are more likely to break out of the main flow in the direction of the gravitational force.
3. Particles with a centrally situated center of mass, like the *LSP,sim*, show an overall slower velocity and a higher likelihood of changing their flow direction, as they tend to convert kinetic energy into rotational energy, which slows them down. Especially the axial velocity is decreased.

These findings support the results described herein for the *LSP,sim*, such as the higher probability of presence in the less turbulent upper region of the STR, and their ability to remain suspended in this region due to their increased likelihood of being reflected by the turbulent zone occurring in the discharge flow of PBT-6 and RT-6. From a statistical point of view, it is worth mentioning that both datasets *LSP,exp* and *LSP,sim* represent a non-ergodic system. Although they have the same number of data points, they differ in the number of LSPs, their respective trial time, and distance traveled in the reactor (Table 3), which could also be a factor in the presented results.

3.4. Circulation time distribution

The evaluation of the circulation time distribution (CTD) is a widely used method to obtain information about the axial homogeneity of

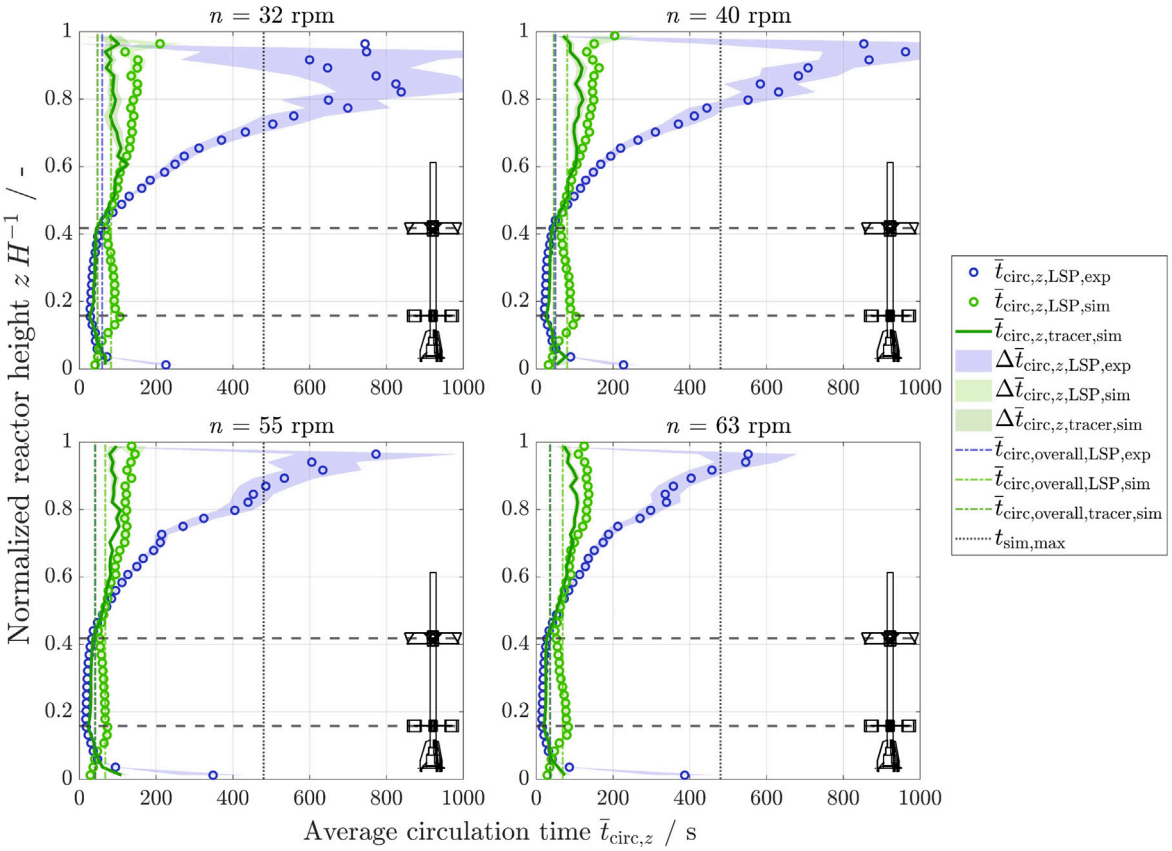

Fig. 9. Average circulation time distribution $\bar{t}_{\mathrm{circ},z}$ as a function of the normalized reactor height z (H = 4.2 m) for experimental LSPs (*LSP,exp*, blue circles), simulated LSPs (*LSP,sim*, green circles), and for simulated tracers (*tracer,sim*, green line), each for $n \in \{32, 40, 55, 63\}$ rpm. The vertical bin size is 10 cm. The shaded areas depict the uncertainty Δ of the respective dataset, the vertical dotted gray line marks the physical simulation time, and the vertical dash-dotted lines denote the overall circulation time $t_{\mathrm{circ,overall}}$. The gray dashed lines indicate the center position of the RT-6 (lower) and PBT-6 (upper). (For interpretation of the references to color in this figure legend, the reader is referred to the web version of this article.)

Table 3
Summary of maximum traveled distances for each rpm case for all experimental LSP runs (*LSP,exp*), simulated LSPs (*LSP,exp*) and simulated, undisturbed tracers (*tracer,sim*) for a total of M trials each.

Particle type	Impeller frequency n / rpm			
	32	40	55	63
$\tilde{d}_{\mathrm{travel,LSP,exp}}$ / m ($M \geq 14$)	381.3 ± 8.6	460.8 ± 17.2	603.0 ± 22.9	661.0 ± 33.2
$\tilde{d}_{\mathrm{travel,LSP,sim}}$ / m ($M = 98$)	26.0 ± 0.3	30 ± 0.5	38.2 ± 0.7	40.4 ± 0.6
$\tilde{d}_{\mathrm{travel,tracer,sim}}$ / m ($M = 98$)	39.2 ± 1.0	45.3 ± 1.3	58.4 ± 1.4	69.8 ± 1.8

the macromixing process within an STR [81], conducted primarily by means of the tracer injection method, for example, measuring the conductivity at a limited number of points [82]. Nonetheless, numerous publications have proved that LSPs may deliver not only the CTD over the reactor height of large tanks, but important data such as general flow structures and hydrodynamic compartments [28,32,76,83,84].

Fig. 9 shows the CTD over the normalized reactor height for the four rpm cases $n \in \{32, 40, 55, 63\}$ rpm with their respective overall weighted average $\bar{t}_{\mathrm{circ,overall}}$ (Table 4). Interestingly, the four undisturbed tracer trends (green line) differ only marginally from each other, which is reflected in the small overall average circulation time difference of ≈ 12 s between the lowest and highest impeller frequency. The lowest circulation time is at the height of the RT-6, which marks the turnover point in the reactor [68]. Both trends of the tracers and the experimental LSPs (blue dots) have similar low circulation times between the impellers and similarly increasing toward the reactor bottom. Even so, their values split at a height of $z\,H^{-1} \approx 0.5$, from which the *LSP,exp* circulation times increase by up to 30 times higher values, compared to the high turbulent zone. At a normalized height of $z\,H^{-1} \approx 0.8$, the trend shows unsteadiness at all impeller frequencies, with values increasing more slowly. The high uncertainties are attributed to the sparse number of data points in the upper third of the STR (Fig. 8). The trends of the simulated LSPs (green dots) demonstrate a peak at the height of the RT-6, with dropping values toward the PBT-6, and again increasing values above the latter toward the top of the reactor. Hence, the peak at the RT-6 denotes a boundary, which they cross less often. The lowest circulation times are in the dished bottom of the STR, which might be due to their clustering behavior and short turning circles. Surprisingly, their distinctive peaks are at the same heights, where the other two types of particles show either their lowest values ($z\,H^{-1} \approx 0.15$) or start to increase sharply ($z\,H^{-1} \approx 0.45$). In summary, the CTDs and their respective overall average values are similar to those of previous work in the same reactor, which was equipped with three Elephant Ear impellers [32].

Small circulation times indicate small and fast turning circles, also in the form of vortices, and thus are reflected as well-mixed zones. Vertical hydrodynamic compartments can be determined at heights, where $\bar{t}_{\mathrm{circ},z}$ increases more rapidly toward higher values, just below RT-6 at $z\,H^{-1} = 0.15$ and above PBT-6 between $0.45 < z\,H^{-1} < 0.55$. Notably, the *LSP,sim* and the CTD of the tracers do not increase as rapidly toward the reactor top as the *LSP,exp*. The main reason is most likely due to the physical simulation time of $t_{\mathrm{sim,max}} = 480$ s (vertical dotted gray line) and the resulting shorter maximum traveled distance compared to the experiments (Table 3). Hence, their CTD must be interpreted with caution with regards to their amount of data and the length of experiments, as was explained by Mann et al. and Day [84,85].

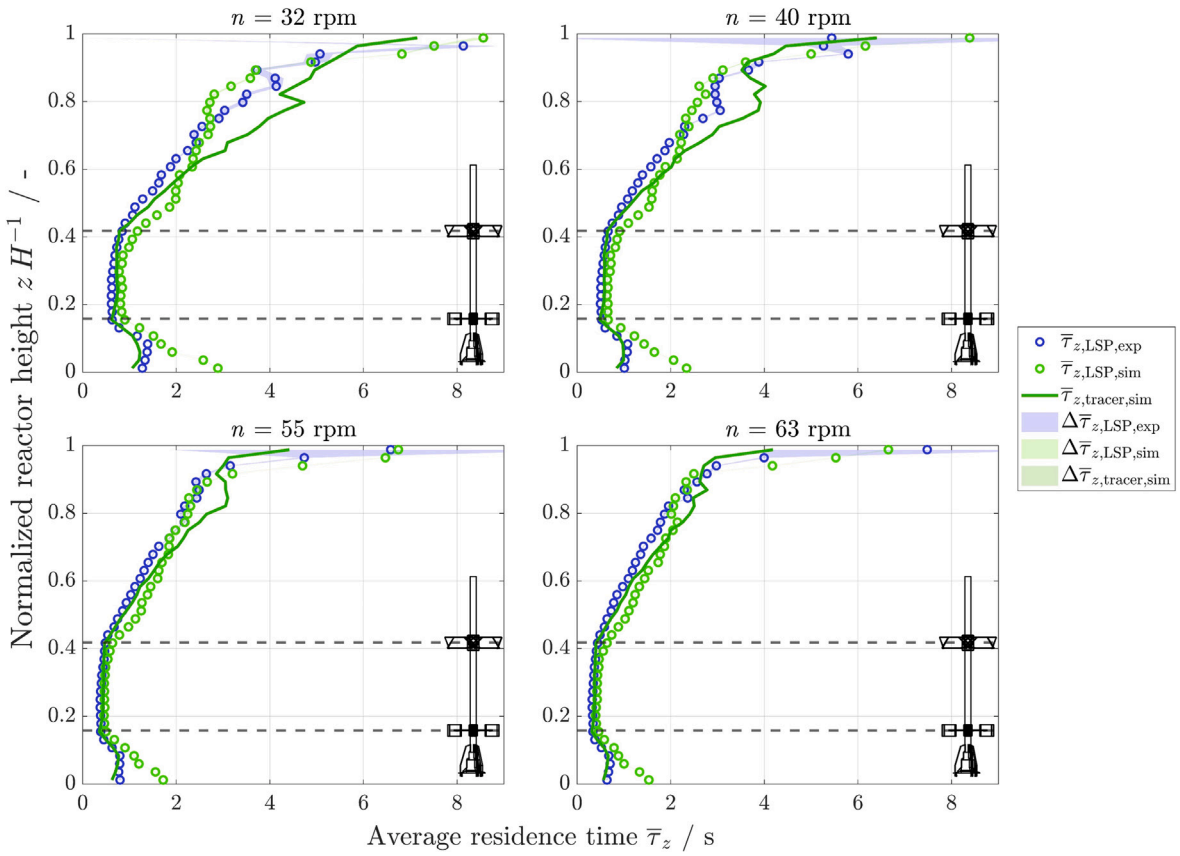

Fig. 10. Average residence time distribution $\overline{\tau}_z$ as a function of the normalized reactor height z ($H = 4.2$ m) for experimental LSPs (*LSP,exp*, blue circles), simulated LSPs (*LSP,sim*, green circles), and for simulated tracers (*tracer,sim*, green line), each for $n \in \{32, 40, 55, 63\}$ rpm. The vertical bin size is 10 cm. The shaded areas depict the uncertainty Δ of the respective dataset, and the vertical dash-dotted lines denote the overall average residence time τ_{overall}. The gray dashed lines indicate the center position of the RT-6 (lower) and PBT-6 (upper). (For interpretation of the references to color in this figure legend, the reader is referred to the web version of this article.)

It appears that the maximum circulation times that occur for both *LSP,sim* and *LSP,exp* are a fourth of the respective maximum trial length. The maximum traveled distance is approximately 15 times higher for *LSP,exp*.

3.5. Residence time distribution

The average hydraulic residence time distribution (RTD) provides information about the tracer's and LSP's average duration in the respective reactor slice j, each with a height of 0.1 m, based on their measured absolute average axial velocity. With regard to the investigation of population heterogeneity within a bioreactor and the classification of cell productivity regimes, this information is vital to conceptualize, manufacture, and evaluate a suitable scale-down reactor design. Laboratory-scale reactors are able to simulate large-scale conditions to understand the interplay between the stress on the microorganism and the resulting product limitations [5,15,19,86,87].

Fig. 10 shows the average residence time distribution over the normalized reactor height for all impeller frequencies $n \in \{32, 40, 55, 63\}$ rpm. The tracer particles' (green line) shortest average residence times are at the height of the RT-6 (lower gray dashed line) with slightly increasing values toward the PBT-6. Below and above the impellers, the residence times are two-fold or even 10-fold higher, respectively. At all impeller frequencies, the trend shows an anomaly between $0.7 < z\,H^{-1} < 0.9$, which is barely seen for *LSP,sim* (green dots), but fairly so for *LSP,exp* (blue dots). However, a similar behavior is observed at the average circulation times of *LSP,exp* at the same height (Fig. 9). Most likely, two fluid flows converge at this height: the direct upward flow from the baffles, which reflects at the liquid surface back downward, and a counteracting, non-directional short-circuit flow. The RTD of the experimental LSPs is similar to the tracer's, although their values start to differ slightly above the PBT-6 to smaller residence times. Nonetheless, in particular, for increasing impeller frequencies, both show good agreement. On the other hand, although the residence times of the *LSP,sim* between the impellers are alike the other two particle types, they show increasing values toward the bottom of the reactor and discontinuous trends toward the top. In summary, all three trends show a distinctive region with comparatively low residence times between $0.15 < z\,H^{-1} < 0.45$ and rapidly increasing values below and above, respectively, which marks vertical hydrodynamic compartment barriers. Compared to a previous study in the same reactor, equipped with three Elephant Ear impellers, the RTD values, as well as the overall cumulative residence times, are similar (Table 4), in particular for low impeller frequencies [32].

Table 4
Overview of results of average overall circulation times, overall cumulated residence times, global mixing times, and respective uncertainties.

Time	Particle type	Impeller frequency n / rpm				
		24	32	40	55	63
$\bar{t}_{\text{circ,overall}}$ / s	*LSP,exp*	–	59.4 ± 2.7	49.7 ± 2.1	40.8 ± 1.6	36.4 ± 1.3
	LSP,sim	–	85.0 ± 0.9	82.4 ± 0.8	70.3 ± 0.6	69.5 ± 0.6
	tracer,sim	–	48.4 ± 0.7	46.4 ± 0.7	42.2 ± 0.5	35.7 ± 0.4
$\overline{\tau}_{\text{overall}}$ / s	*LSP,exp*	–	81.1 ± 2.5	73.2 ± 7.6	56.9 ± 5.4	52.6 ± 4.0
	LSP,sim	–	99.5 ± 1.0	83.7 ± 0.7	69.1 ± 0.6	63.3 ± 0.5
	tracer,sim	–	99.9 ± 0.8	81.2 ± 0.6	59.3 ± 0.4	52.7 ± 0.4
$\Theta_{\text{glob,95}}$ / s		247 ± 14	191 ± 5	151 ± 9	106 ± 3	102 ± 13

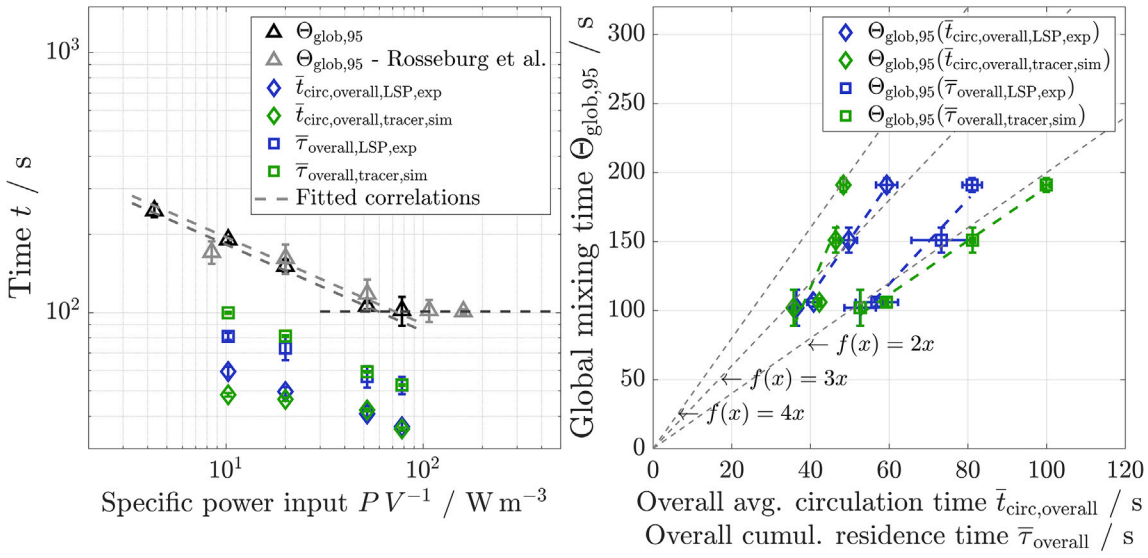

Fig. 11. Left: Measured global mixing times $\Theta_{glob,95}$ (black triangles), global mixing times from Rosseburg et al. in the same reactor setup (gray triangles) [43], overall average circulation times $\bar{t}_{circ,overall}$ (diamonds), and overall cumulated residence times $\bar{\tau}_{overall}$ (squares) as a function of the specific power input PV^{-1}. For the last two, values for experimental LSPs (*LSP,exp*, blue) and for simulated tracer (*tracer,sim*, green) are shown. Dashed lines are literature correlations. Right: Global mixing time as a function of overall average circulation time and overall cumulated residence time with a respective linear correlation for experimental LSPs (blue) and tracer (green). (For interpretation of the references to color in this figure legend, the reader is referred to the web version of this article.)

Table 5
Overview of empirical mixing time correlations from literature for multi-staged impellers in an unaerated STR.

Correlation	Comment	Author
$\Theta_{glob} = B \cdot Po^{-1/3} \cdot \left(\frac{n}{60}\right)^{-1} \left(\frac{H}{d_{STR}}\right)^{2.43}$	B: fitting const.; here: 2.1	Cooke et al. [94]
$\Theta_{glob} = B \cdot \left(\frac{d_{STR}}{d_{imp}} \cdot \bar{\varepsilon}_T\right)^{-1/3} \cdot \left(\frac{H}{d_{STR}}\right)^{2/3} \cdot (N_{imp}+1)^{2/3}$	B: fitting const.; here: 16.5	Sieblist et al. [95]
$n \cdot \Theta_{glob,95} = 2.3 \cdot \exp\left(0.68 \cdot \frac{d_{STR}}{d_{imp}} + 0.83 \cdot N_{imp}\right)$		Vasconcelos et al. [96]

3.6. Mixing times

In a fed-batch cultivation of animal cells, nutrients are added according to precise feeding strategies after being metabolized to achieve optimal product yield and titer. [88]. Process intensification strategies, such as perfusion processes, result in very high cell densities, yet require a high degree of homogeneity throughout the reactor [8]. Therefore, mixing time is a key parameter as it is critical for cell growth and, eventually, for the quality and quantity of the product. Moreover, it is a core characterization parameter for a bioreactor and serves as both a modeling parameter and a validation measure for numerical simulations, in particular for scale-up and scale-down strategies [60,82,89–92]. In this study, the decoloration method by means of utilizing bromothymol blue (BTB) is evaluated according to Paul et al. [74] at a 95% mixedness. The contrasting color change of the BTB and the resulting logarithmic variance of the normalized gray scale enables a detailed temporal progress of either the STR as an entirety (global mixing time $\Theta_{glob,95}$) or highly resolved (local mixing time distribution $\Theta_{loc,95}$) [93] for a compartment localization. The basic methodology of the latter is elucidated in Fitschen et al. [59].

In Fig. 11 (left), the global mixing times measured $\Theta_{glob,95}$ from this study (black triangles, Table 4) and from a previous study (gray triangles) by Rosseburg et al. [43] are plotted as a function of the specific power input. The latter were obtained in the same reactor ($V = 12.0\,m^3$, $H\,d_{STR}^{-1} = 2.0$) by means of the decoloration method with phenolphthalein. All values agree well with the correlations given by Cooke et al. [94] (light gray dashed line) and Sieblist et al. [95] (dark gray dashed line), if taking into account the fitting constants $B = 2.1$ and $B = 16.5$, respectively (Table 5). The horizontal dashed line denotes a range in which, according to Zlokarnik, the mixing time is independent of the stirrer speed [57]. This smallest possible mixing time seems to be $\Theta_{glob,95} \approx 100$ s. Furthermore, global mixing times from a recent study on hydrodynamic stress in the identical reactor fit in the same correlation [13], as well as the results from Bernemann et al. [90] (not shown here). In addition, overall average circulation times (diamonds) and overall cumulative residence times (squares) are plotted in the same graph for the experimental LSPs (*LSP,exp*, blue) and for the tracer particles (*tracer,sim*, green) as a reference point. Their trends demonstrate similar behavior. With an increasing power input, their values align within a comparatively low uncertainty. The primary reason for the discrepancy in low PV^{-1} values is mainly due to their difference in recording length (Chap. 3.4) and a combination of limited data points for *LSP,exp* and elevated residence times within the fluid reflection zone in the top of the reactor (Chap. 3.5), respectively.

Fig. 11 (right) shows the overall average circulation times (diamonds) and the overall cumulated residence times (squares) in the context of their respective global mixing time with a linear regression for the experimental LSPs (*LSP,exp*, blue) and for the tracer particles (*LSP,sim*, green). The circulation time ratios are shown to be $2.6 \cdot \bar{t}_{circ} < \Theta_{glob,95} < 4.0 \cdot \bar{t}_{circ}$, depending on the particle type, where the tracer data have a higher ratio in part than the experimental data, due to their limited physical time in the reactor. The ratio of the overall cumulated residence time is for both particle types approximately between 2 and 2.4. In particular, in the case of circulation times, previous studies report of $3 \cdot t_{circ} < \Theta_{glob,95} < 5 \cdot t_{circ}$ with conductivity measurements and a single-staged RT-6 ($H\,d_{STR}^{-1} = 1.0$) [60,97–99]. The lowest ratio is presented by Bisgaard et al. with $\Theta_{glob,95} = 2.2 \cdot t_{circ}$ [76]. Another work, which exclusively uses three axial pumping impellers (Elephant Ear, ABEC design) on industrial scale with a $H\,d_{STR}^{-1} = 2.1$ reports of $1.1 \cdot t_{circ} < \Theta_{glob,95} < 1.5 \cdot t_{circ}$, similar to a model approach by van de Vusse [100]. Hence, the results of this study coincide well with the results of the literature, considering an RT-6 and a PBT-6 with $H\,d_{imp}^{-1} = 2.1$.

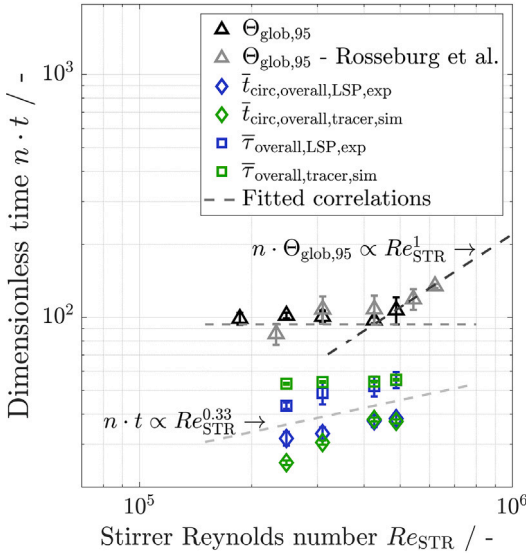

Fig. 12. Dimensionless time $n{\cdot}t$ as a function of the stirrer Reynolds number Re_{STR} with $t = \Theta_{glob,95}$ as dimensionless mixing time (black triangles), $t = \bar{t}_{circ,overall}$ as dimensionless circulation time (diamonds), and $t = \bar{\tau}_{overall}$ as dimensionless residence time (squares). For the last two, the experimental LSPs (*LSP,exp*, blue) and tracer (*tracer,sim*, green) are shown. Linear correlations are depicted as dashed lines. (For interpretation of the references to color in this figure legend, the reader is referred to the web version of this article.)

Aforesaid results can be displayed via dimensionless time ($n \cdot t$) as a function of the stirrer Reynolds number Re_{STR} [57], together with widely used correlations found in the literature (Table 5). Fig. 12 indicates all the experimental results of the mixing times (triangles), overall average circulation times (diamonds), and overall cumulated residence times (squares). As described by Zlokarnik [57], the mixing time results at given Reynolds numbers in this study can be subdivided into two ranges. The first range is $n{\cdot}\Theta_{glob,95} = \text{const.}$, below the Reynolds numbers $Re_{STR} < 4.3 \cdot 10^5$, which coincides with the correlation by Vasconcelos et al. [96] (Table 5). This range is also described and analyzed in other publications [95,101–103]. With an increasing impeller frequency, and thus higher Reynolds numbers $Re_{STR} > 4.3 \cdot 10^5$, the correlation changes to $n \cdot \Theta_{glob,95} \propto Re^{1}_{STR}$ in the second range, also described by Rosseburg et al. [43] and Gabelle et al. [104]. Any other mixing time correlation found describes either a setup with only one single impeller type or an STR with mostly $H\, d^{-1}_{STR} = 1$ [74,102,105,106]. Interestingly, the experimental overall average circulation time and overall cumulated residence time do not obey this correlation. They indicate $n \cdot \Theta_{glob,95} \propto Re^{0.33}_{STR}$, at least with the limited number of data points.

A more detailed analysis is demonstrated in Fig. 13, which shows the relative local mixing time distribution Θ^* throughout the reactor at four impeller frequencies $n \in \{32, 40, 55, 63\}$ rpm. According to Eq. (32), the calculated local mixing time in a $2\,x\,2$ pixel array is normalized by the respective global mixing time $\Theta_{glob,95}$. From a qualitative point of view, three compartments are formed in the STR: one in the bottom of the reactor, below the RT-6 at $z\,H^{-1} \approx 0.15$, the second between the RT-6 and the vertical center of the reactor at $z\,H^{-1} \approx \{0.54, 0.49, 0.44, 0.49\}$, and a third compartment in the top region. An overall similarity of the relative mixing time distributions reveals that prevailing compartments are almost independent of the impeller frequency, as was also reported in an earlier work in a 3 L STR [107]. For the first time, detailed hydrodynamic compartments on industrial scale are illustrated based on mixing time experiments, and demonstrate a high agreement with the aforementioned LSP results (Chap. 3.2, 3.4, 3.5), and furthermore, a number of foregoing experiments [108] and numerical simulations regarding this topic [63,109]. However, evaluating mixing times in an industrial-scale acrylic glass STR contains challenges and causes errors. Although sufficient and homogeneous background lighting is provided, one wide-angle lens at the designated height and distance creates distortion, in particular toward the top of the reactor. For cylinder imaging evaluations, it is recommended to work with refraction compensation [110], which can be achieved by implementing containers outside [34,90], albeit not realistic for this reactor size. Moreover, outer obstacles or moving objects, such as cross beams, tank nozzles, acrylic glass flanges, the stainless steel dished tank bottom, and impellers, hinder an evenly illuminated view of the inside. Nevertheless, suitable post-processing steps yield a spatio-temporal resolved 2D map that highlights coherent structures primarily influenced by mixing.

3.7. Lagrangian regime analysis

Substrate gradients in industrial bioreactors affect the cell's biokinetics and metabolic dynamics, leading to population heterogeneity (changes in the metabolome, proteome and transcriptome) and eventually to a decline in growth and production [5,111,112]. Therefore, lifeline analysis has become a valuable tool for developing scale-down simulator concepts or even microfluidic chips in order to mimic large scale conditions on a laboratory scale [19,113,114]. The Euler–Lagrange concept was introduced by Lapin et al. [30] and has gained attention in recent years [31]. Haringa et al. presented three Lagrangian analysis methods to interpret a particle's trajectory, of which this study applies the *Lagrangian regime analysis* [115,116].

The discretization of the Lagrangian trajectories from all three particle types provides the residence times in the ascertained single-phase hydrodynamic compartments τ_{regime}, which is depicted in Fig. 14, exemplary for $n = 55$ rpm. The compartment barriers at $z\,H^{-1} = 0.15$ and $z\,H^{-1} = 0.44$ are set based on the results in the previous chapters, the CTD, RTD, and local mixing time distribution. Residence times in the upper (red), center (green), and lower compartments (blue) are shown with their probability density. It is seen that *LSP,exp* (upper) and *LSP,sim* (center) show a contrasting probability of residence times until $\tau_{regime} \approx 20$ s for the upper and lower compartment. This behavior can be explained by their different probability of presence over the reactor height (Fig. 8). In addition to that, both trends are generally in good agreement with the tracer results (*tracer,sim*, lower). However, a substantial condition might arise at probabilities greater than $\tau_{regime} > 117$ s (vertical dashed line) in the upper compartment, which is a theoretically calculated limit for a Chinese Hamster Ovary (CHO) cell to be oxygen-deprived [32], especially at high biomass concentrations. Associated studies with CHO cells were conducted by Gaugler et al. and Anane et al. [19,25]. When exposed to dissolved oxygen gradients, they report a more rapid decline in viable cell count and an increase in lactate concentrations.

In summary, the findings indicate a 0.1%, 2.3%, and 1.3% probability that the *LSP,exp*, the *LSP,sim*, or *tracer,sim*, respectively, will remain longer in the upper compartment than the theoretical limit allows. With a lower limit of oxygen deprivation of 90 s, the probabilities increase to 0.4%, 4.2%, and 1.7%, respectively. The *LSP,exp* slightly underrepresented the tracers' probability, notwithstanding their longer maximum travel distance during a trial, owed to their decreased probability of presence in the top of the STR.

3.8. Stokes number estimations

Lagrangian Sensor Particles are large, nearly neutrally-buoyant particles that move with the turbulent surrounding carrier flow in a characteristic way. Their size is three orders of magnitude larger than the Kolmogorov length scale and approximately one order of magnitude larger than the Taylor scale. Due to their high inertia, the resulting drag causes a relevant reaction time lag to changes in fluid velocity [50]. In the context of flow-following characteristics and for classification benefits, this study offers various methodologies to estimate the Stokes

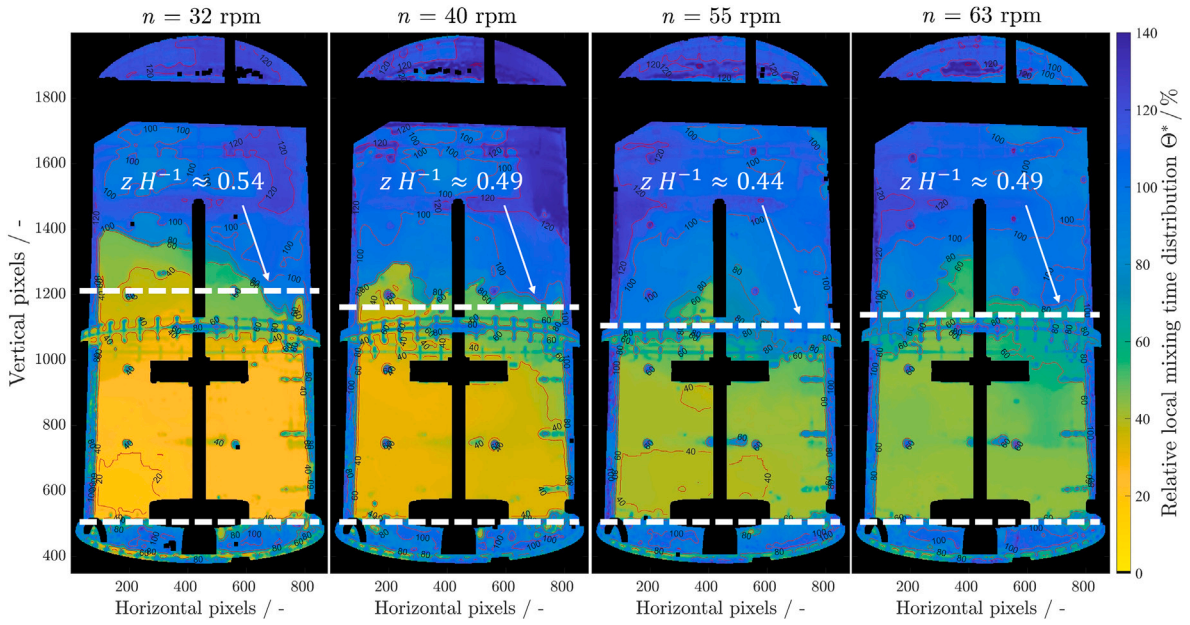

Fig. 13. Comparison of relative local mixing time distributions Θ^* (local mixing time $\Theta_{loc,95}$ in a 2 × 2 pixel array normalized by the respective global mixing time $\Theta_{glob,95}$) at four impeller frequencies $n \in \{32, 40, 55, 63\}$ rpm. The global mixing times are $\Theta_{glob,95} \in \{191 \pm 5, 151 \pm 9, 106 \pm 3, 102 \pm 13\}$ s, respectively. The injection point (IPO) is marked in Fig. 1. Due to the recording distance of the camera, the camera lens used, and the resulting image distortion, pixels are specified instead of distances.

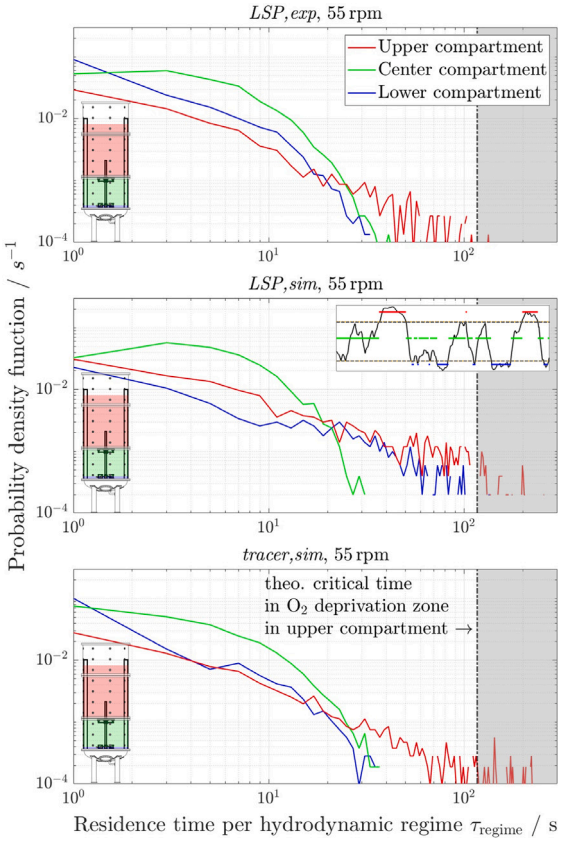

Fig. 14. Probability density function of the residence time per hydrodynamic regime τ_{regime} for the upper (red), center (green) and lower (blue) regime for the experimental LSPs (*LSP,exp*), simulated LSPs (*LSP,sim*) and tracer (*tracer,sim*) at $n = 55$ rpm. Compartment barriers are taken from CTD, RTD and relative local mixing time distributions at $z\,H^{-1} = 0.15$ and $z\,H^{-1} = 0.44$. The vertical dashed line and gray area indicates a theoretical time limit at 117 s for a CHO cell to be oxygen limited. Inset: Exemplary trajectory discretization with the respective compartment color. (For interpretation of the references to color in this figure legend, the reader is referred to the web version of this article.)

number; however, it does not adequately predict the dynamics of LSPs of this magnitude [61,117]. Generally, this research outlines three approaches for Stokes number estimations based on the underlying data and the assumptions made. The results are listed in Table 6.

The first approach utilizes only the experimental axial velocity data obtained to calculate the slip velocity in Re_p and the resulting drag coefficient to estimate τ_p (Eq. (8)). The large eddy turnover times τ_f are calculated with Eqs. (12)–(14) so that the calculated Stokes numbers are approximately two orders of magnitude apart from each other (Table 6, upper part). Obviously, the used LSPs with a diameter of $d_p = 40$ mm demonstrate a minor flow-following behavior on the micro-scale; however, a Stokes number of St (meso-scale) ≈ 0.2 indicates that they are indeed able to detect compartment barriers and heterogeneities on the meso-scale, as the previous chapters impose, in particular concerning the local mixing time distribution. On the macro-scale, the LSPs show similar results to the simulated undisturbed fluid flow tracers regarding the overall average circulation time (Fig. 11). This similarity is due to the comparatively short physical time in the STR of the latter, which explains the low St (macro-scale) ≈ 0.002. Hence, this approach provides a fair assessment of the LSPs utilized by applying only experimental data.

The second and third approaches utilize only numerical simulation data and differ in their way of calculating the slip velocity and eventually demonstrating the final data: either as a single stochastic value, which removes the bias and focuses on fluctuations [61] or as a detailed 2D distribution with bin size L representing the mean flow (MF) [32]. In Table 6 (center), the stochastic values are stated. The 2D distributions are shown in Fig. 15, whereupon the respective average values are also indicated in Table 6 (lower part). Both approaches are able to calculate the Stokes number and, in addition, a theoretical maximum particle diameter, which would actually be able to follow the flow with the given fluid velocity data in the STR [34]. In that case, a Stokes number of $St = 0.1$ is assumed [53], according to which the term $(c_D\, Re_p)/24$ approaches unity, since now Stokes drag applies [118]. The theoretical particle diameter is calculated as

$$d_{p,th} = \sqrt{\frac{18\, St\, \eta\, L}{\rho_p\, \boldsymbol{u}}}, \tag{33}$$

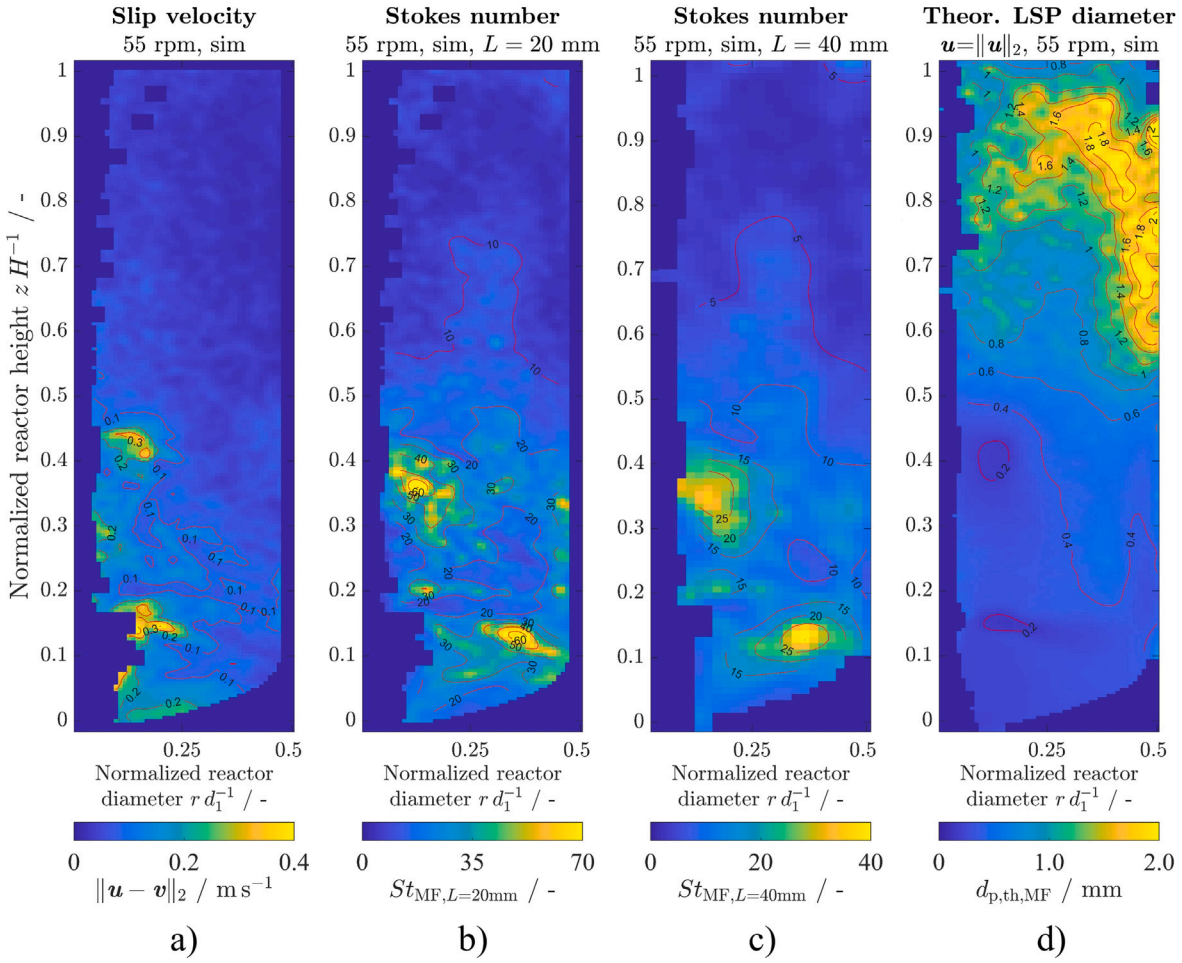

Fig. 15. Numerical data results depicted as a 2D distribution in a predefined bin size L representing the mean flow (MF) for an impeller frequency of n = 55 rpm for both simulated particle types *LSP,sim* and *tracer,sim*. (a) The slip velocity distribution calculated by means of the second euclidean norm with L = 20 mm. (b) The consequent Stokes number distribution St_{MF} with L = 20 mm. (c) The Stokes number distribution with a doubled L = 40 mm. (d) Theoretical, maximum particle diameter $d_{p,th,MF}$ to comply with the flow-following criterion according to St = 0.1. All data is time-, axially- and azimuthally-averaged.

Table 6
Overview of results of Stokes number estimations on different scales, approaches and respective equations, calculated slip velocities and estimated theoretical particle sizes necessary to be flow-following in the STR.

		Equations	Impeller frequency n / rpm			
			32	40	55	63
experimental	St (micro-scale) / –	(8), (14)	29.4	34.2	41.3	42.9
	St (meso-scale) / –	(8), (12)	≈ 0.20			
	St (macro-scale) / –	(8), (13)	≈ 0.002			
LB LES	$\boldsymbol{V}_{slip,stoch}$ / m s^{-1} (·10^{-2})	(15)	8.6	10.4	13.5	17.0
	St_{stoch} / –	L = 20 mm, (15), (16)	1.2	1.4	1.9	2.0
	$d_{p,th,stoch}$ / mm	(33), $\boldsymbol{u} = u_{stoch}$	1.5	1.3	1.0	0.8
LB LES	$\overline{\|\boldsymbol{u}-\boldsymbol{v}\|_2}$ / m s^{-1} (·10^{-2})		5.4	6.4	7.9	8.9
	$\overline{St}_{MF}$ / –	L = 20 mm, (17)	13.9	13.9	15.6	16.1
	$\overline{d}_{p,th,MF}$ / mm	(33), $\boldsymbol{u} = \|\boldsymbol{u}\|_2$	0.9	0.8	0.7	0.7

which again delivers either a single stochastic value $d_{p,th,stoch}$, or a 2D distribution based on the mean flow grid of L = 20 mm and its average value $\overline{d}_{p,th,MF}$.

As shown in Table 6, the stochastic Stokes number St_{stoch} is approximately one order of magnitude underestimated compared to the average Stokes number of the mean flow $\overline{St}_{MF}$ of the 2D distribution. The theoretical maximum particle sizes are in good agreement, particularly with increasing impeller speed.

The 2D distributions in Fig. 15 yield a detailed insight into the hydrodynamics of the STR. The highest slip velocity and, thus, the highest Stokes numbers are found in the vicinity of the impellers. It should be mentioned that the size of the Stokes number obviously scales with the chosen size of the characteristic length scale L in τ_f, which is chosen as L = 20 mm (Fig. 15 (b)) and L = 40 mm (Fig. 15 (c)) for comparison reasons. Interestingly, the estimated experimental Stokes number on the micro-scale St (micro − scale) = 41.3 (Table 6) is in a similar range as the Stokes number of the *LSP,sim* in the 2D distribution (Fig. 15 (b)) near the impellers, especially if the Stokes number proposed by Rautenbach et al. with the center of mass shift factor of r^* = 0.79 is incorporated [33]. Moreover, the theoretical particle sizes to fulfill the Stokes criterion are the lowest in the vicinity of the impellers with $d_{p,th,MF} \approx 0.2$ mm and increase up to 2.0 mm with increasing distance. The bulk phase would be covered with an LSP size of approximately 1 mm, in order to theoretically follow the flow on a micro-scale, based on the characteristic length of the mean flow of L_{MF} = 20 mm. Interestingly, in a previous publication, which utilized 4D-Particle Tracking Velocimetry and accompanying LB LES in a 3 L STR, similar values were predicted for the industrial scale for a similar specific power input [34].

4. Conclusions

This study represents an analysis of experimentally and numerically derived particle trajectories to hydrodynamically characterize

a single-phase industrial bioreactor for heterogeneities and compartments occurring at different impeller frequencies. The stirred tank reactor (STR) is equipped with a Rushton turbine (RT-6) and a pitched blade turbine (PBT-6) and constitutes an industrial replica with a filling volume of 12.5 m^3, made of acrylic glass. Regarding particle trajectories, on the one hand, Lagrangian Sensor Particles (*LSP,exp*), outfitted with a pressure sensor, yield the experimental time-resolved axial height. On the other hand, resolved particle Lattice-Boltzmann large eddy simulations (LB LES) are utilized to emulate those LSPs in the same STR (*LSP,sim*). Furthermore, they provide undisturbed fluid flow data by means of massless tracer particles (*tracer,sim*), which serve as a reference when elucidating the LSP results. The main goal is to prove the technological readiness of LSPs, discuss their size and number in the STR, and provide crucial information about future evaluations.

This work finds that the contrary behavior in the axial probability of presence over the reactor height between *LSP,exp* and *LSP,sim* is most likely due to four main facts. Firstly, the difference in their mass distribution; secondly, their slightly different density; thirdly, the particle number in the reactor; and fourthly, most likely a sufficient but improvable particle-to-grid size ratio. As demonstrated in Rautenbach et al. LSPs with a homogeneous mass distribution, such as used in the simulation for *LSP,sim*, show a decisively higher probability of presence in less turbulent regions and less momentum required to correspond to instantaneous changes in fluid flow [33]. Moreover, the slightly higher density of *LSP,sim* of 0.7 $kg\,m^{-3}$ provides them with a higher cluster probability in the bottom of the STR, and additionally, an increasing particle collision and perturbation probability of at least 4% due to their high number of particles in the reactor. Due to the high computational demand, the number of particles had to be increased to approximately 250 to reach the same physical trial time (13 h in total per dataset), instead of utilizing only a maximum of three LSPs at the same time for a period of 1 h each (in the case of experiments). Beyond, the particle-to-grid size ratio of 10 might be still too little to accurately calculate the two way coupled fluid–particle forces in the computational boundaries in the lattice structure. Generally, by representing the data density over the reactor height, that information helps understanding the upcoming results.

The aforementioned results on the axial probability of presence in combination with the accompanying sensitivity study outline the axial velocity difference between *LSP,exp* and *LSP,sim*. The latter exhibit higher probabilities for slow velocities, likely due to their comparatively higher probability of presence in the upper reactor zone, which is less turbulent. Furthermore, the high particle volume fraction utilized in the LB LES increases collisions and clustering, attenuates the carrier flow according to the decrease in velocity fluctuations, reduces turbulent kinetic energy by at least 3%, and ultimately leads to a decrease in the LSP's velocity. To avoid these effects, a maximum particle volume fraction of $\approx 10^{-4}$ should not be exceeded for future experiments. Moreover, the homogeneous mass distribution of *LSP,sim* makes them more responsive to horizontal flow changes, resulting in slower axial velocities. However, except for very high velocities, which are obviously characteristic fluid speeds near the impeller blades, both LSP types generally show good agreement.

Furthermore, this work elaborates that the CTDs of *LSP,exp* and *tracer,sim* look alike below the vertical center of the reactor. A distinctive high-turbulent region with small circulation times marks a compartment with two boundaries, below the RT-6 and just above the PBT-6. Above the latter, *LSP,exp* demonstrate 30-fold higher circulation times, owing to their low probability of presence in the upper reactor region and a slight density difference. Since the physical time of the simulated particles is only 480 s, compared to 3600 s for *LSP,exp*, the average circulation times of both LSP types, experimental and simulated, are hardly comparable in this region.

The distributions of the residence times are fairly similar for all particle types, marking the same well-mixed region, and thus three horizontal compartments with barriers at the same height as evaluated with the CTD.

Consequently, mixing time trials reveal that global mixing times $\Theta_{glob,95}$ fit in the context of literature results that include different correlations. In particular, the ratio of the overall average circulation times $\bar{t}_{circ}$ of *LSP,exp* and *tracer,sim* agree well with previous publications, as they show $2.6 \cdot \bar{t}_{circ} < \Theta_{glob,95} < 4.0 \cdot \bar{t}_{circ}$, depending on the type of particles. The dimensionless residence times $\overline{\tau}_{overall}$ show $n \cdot \overline{\tau}_{overall} \propto Re_{STR}^{0.33}$. The relative local mixing time distribution Θ^* confirms the three compartments, acquired by means of the CTD and RTD at $z\,H^{-1} \approx 0.15$ and $z\,H^{-1} \approx 0.50$.

The Lagrangian regime analysis utilizes ascertained compartment barriers to discretize the particle trajectories. It further illustrates the probability of how likely it is for the particles, which are supposed to mimic the lifeline of a Chinese Hamster Ovary (CHO) cell, to be situated in an oxygen-deprived zone in the upper STR compartment. With an assumed oxygen deprivation limit of 90 s, *tracer,sim* shows a probability of 1.7%, while the results for *LSP,exp* (0.4%) and *LSP,sim* (4.2%) are respectively under and overestimated due to their characteristic probabilities of presence.

Multiple approaches are presented for the estimation of the Stokes number St, based on the available data and assumptions, and serve as a point of reference. Solely determined with experimental data, with $St \approx 0.20$ on the meso-scale, and $St \approx 0.002$ on the macro-scale, *LSP,exp* demonstrate sufficient flow-following capability to detect hydrodynamic compartments, as is proven in this study. Regarding the Stokes number on the micro-scale of *LSP,sim*, the average of a 2D distribution and the stochastic value are between $13.9 < \overline{St}_{MF} < 16.1$ and $1.2 < St_{stoch} < 2.0$, respectively. Consequently, a theoretical LSP size of $d_{p,th} \approx 1$ mm is calculated, which would satisfy the flow-following requirement of $St = 0.1$ on the micro-scale in the bulk phase of the bioreactor.

Eventually, extending the application of LSPs beyond bioreactors is essential, particularly to evaluate the impact of hydrodynamic heterogeneities on process efficiency and economic performance. Ongoing research within the DFG Collaborative Research Center (CRC 1615 "SMART Reactors for Future Process Engineering") at the Hamburg University of Technology (TUHH) investigates applications in other industrial processes, such as chemical reactors, focusing on particle-laden flows and sensor particle swarms. While this study provides insights into single-phase bioreactor heterogeneities, applying these findings to multiphase systems requires further research due to added complexities like mass transfer and varying bubble size distributions. Related research with LSPs in the Clean Water Technology Lab (CLEWATEC) at the Helmholtz-Zentrum Dresden-Rossendorf (HZDR) examines hydrodynamics in biogas fermentors, which face poor mixing due to highly complex substrates, low height-to-diameter ratios, and varied agitator designs. These studies aim to optimize efficiency and resource usage, although experimental work during the operation of biogas plants is limited by the risk of process instability and economic losses.

To summarize, this study demonstrates that state-of-the-art LSP technology is an effective tool for investigating large-scale stirred tank reactors. The results showcase the capability of LSPs to detect hydrodynamic heterogeneities in the form of compartments, without requiring optical access. Despite their size, LSPs effectively provide mixing data on the meso- and macro-scale, as corroborated by accompanying LB LES and mixing time studies. For a more comprehensive, time-resolved determination of the LSP locations, resolved particle LB LES simulations will be valuable in guiding future LSP designs.

CRediT authorship contribution statement

Sebastian Hofmann: Writing – review & editing, Writing – original draft, Visualization, Validation, Supervision, Software, Resources, Methodology, Investigation, Formal analysis, Data curation, Conceptualization. **Ryan Rautenbach:** Writing – review & editing, Writing

– original draft, Validation, Software, Methodology, Formal analysis, Data curation. **Lukas Buntkiel:** Writing – review & editing, Writing – original draft, Software, Resources, Methodology, Investigation, Conceptualization. **Isabel Sophie Brouwers:** Methodology, Data curation. **Lena Gaugler:** Writing – review & editing. **Jonas Barczyk:** Writing – review & editing. **Jürgen Fitschen:** Writing – review & editing, Methodology. **Sebastian Reinecke:** Writing – review & editing, Project administration, Funding acquisition. **Marko Hoffmann:** Writing – review & editing, Project administration, Funding acquisition. **Ralf Takors:** Supervision, Project administration, Funding acquisition. **Uwe Hampel:** Supervision, Resources, Project administration, Funding acquisition. **Michael Schlüter:** Writing – review & editing, Supervision, Resources, Project administration, Funding acquisition.

Declaration of Generative AI and AI-assisted technologies in the writing process

During the preparation of this work, the authors used "Writefull's model" in "Overleaf" in order to improve the readability of the manuscript. After using this tool, the authors reviewed and edited the content as needed and take full responsibility for the content of the published article.

Declaration of competing interest

The authors declare that they have no known competing financial interests or personal relationships that could have appeared to influence the work reported in this paper.

Acknowledgments

The authors appreciate the funding by the German Research Foundation (Deutsche Forschungsgemeinschaft - DFG) within the Priority Program SPP 2170 "InterZell" (Grant Number: 42789983). Parts of the HZDR's work have been funded by BMEL, Germany, in the SensOMix project (FKZ 2219NR390), and the Neobio project (FKZ 22032618) and by the Helmholtz Association Initiative and Networking Fund, Germany, within the framework of the Clean Water Technology Lab (CLEWATEC) - A Helmholtz Innovation Lab (HIL-A02). Publishing fees supported by Funding Programme Open Access Publishing of Hamburg University of Technology (TUHH). In particular, we thank Marc Maly for proofreading, Felix Kexel for constructive discussions, and Jakob Schulze and Helena Ostrinsky for support during the experiments.

Appendix A. Grid independence study

See Figs. 16 and 17.

Appendix B. Sensitivity study

Fig. 18 depicts the probability densities of the three velocity components for both the fluid (upper) and the LSPs (lower), for the two highest volume fractions at 55 rpm. The single-point statistics are normalized by the respective root mean square component calculated from the tracer in an undisturbed flow (dashed line). With regard to the fluid velocity statistics, interestingly, they seem not affected by the presence of LSPs as no statistically significant differences in the trends can be observed as described similarly in Ouellette et al. and Cisse et al. [70,72]. On the other hand, the particle velocity statistics show a clear dampening effect, in particular for higher velocities. This expected result emphasizes the inertia of LSPs, which is similarly shown in previous studies [34,61]. Both particle types and the undisturbed flow tracer demonstrate a non-uniform, asymmetric, spatial distribution of their velocity components, which emphasizes a large-scale anisotropic turbulence behavior in the entity of the STR. The results of the numerical sensitivity study for all particle volume fractions utilized are summarized in the Table 7.

Table 7
Summary of numerical sensitivity study: Statistical results for all particle volume fractions at $n = 55\,\mathrm{rpm}$.

Particle number/–	18	44	92	155	304
Particle volume fraction $\Phi_{\mathrm{LSP,sim}}(\cdot 10^{-4})$/–	0.48	1.18	2.47	4.16	8.15
τ_c/s	1024	419	200	119	61
$\tau_p\,\tau_c^{-1}\,(\cdot 10^{-2})$/–	0.10	0.24	0.50	0.84	1.65
PCP/%	0.21	3.00	3.66	3.75	7.33
$u^2_{z,\mathrm{rms}}\,(\cdot 10^{-2})/\mathrm{m^2\,s^{-2}}$	5.54	5.14	5.30	5.39	4.72
$u^2_{\theta,\mathrm{rms}}\,(\cdot 10^{-2})/\mathrm{m^2\,s^{-2}}$	5.37	5.40	4.77	5.27	5.06
$u^2_{r,\mathrm{rms}}\,(\cdot 10^{-2})/\mathrm{m^2\,s^{-2}}$	4.29	4.14	4.27	4.13	3.85
$k\,(\cdot 10^{-2})/\mathrm{m^2\,s^{-2}}$	2.51	2.44	2.38	2.44	2.29

Appendix C. Global mixing times

See Fig. 19.

Data availability

Used MATLAB® scripts that are developed in order to evaluate the data can be publicly accessed at the Gitlab project. Raw data and results are publicly accessible in the DaRUS repository. Please contact Sebastian Hofmann, Ryan Rautenbach, or Lukas Buntkiel for further information.

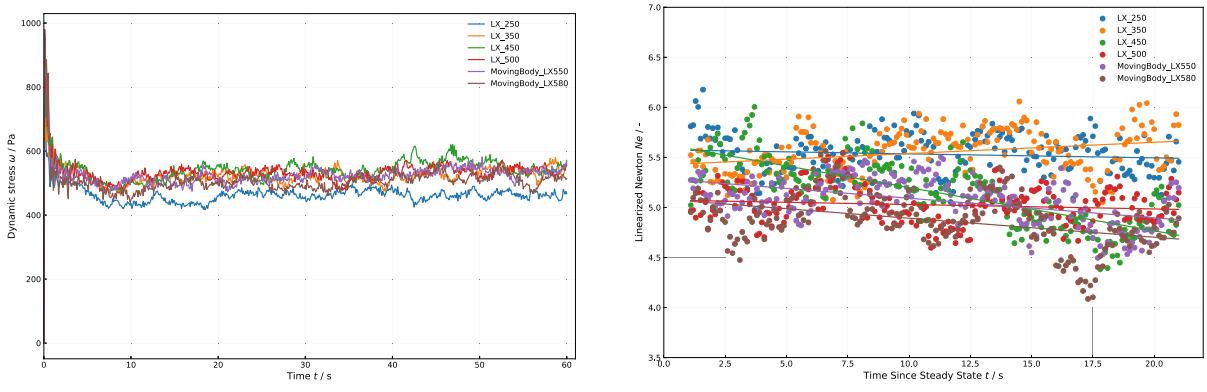

(a) (b)

Fig. 16. Plot (a) showing the dynamic stress over time related to the moving body with an RT-6 and a PBT-6 configuration at different lattice densities and plot (b) of the linearized Power number over time since steady state.

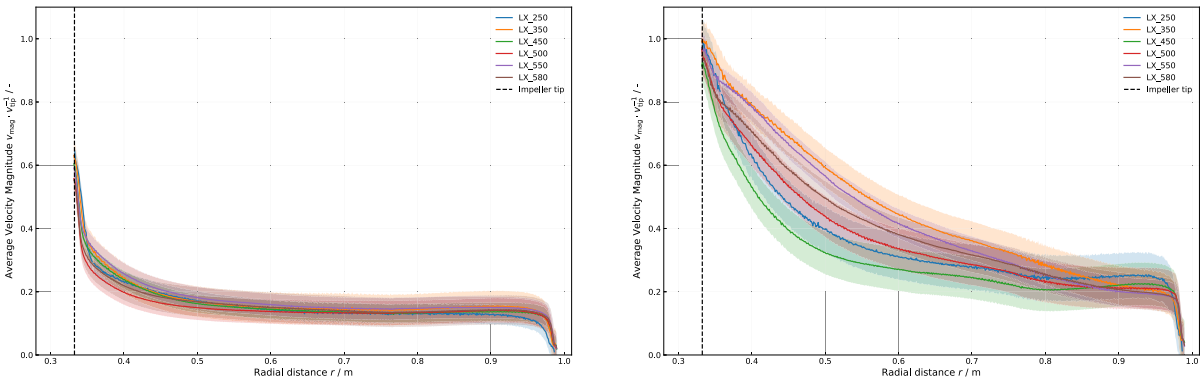

Fig. 17. Plot (a) showing the azimuthal velocity magnitude in the plane of the pitched blade over the radial distance from tip to reactor wall at different lattice densities and plot (b) of the azimuthal velocity magnitude in the plane of the Rushton impeller over the radial distance from tip to reactor wall at different lattice densities.

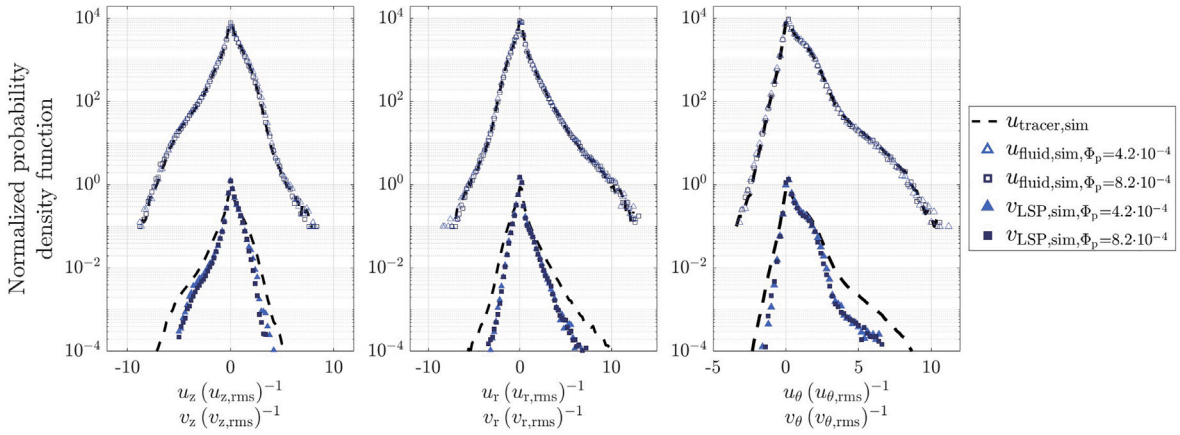

Fig. 18. Normalized probability density of the simulated Lagrangian fluid velocities u (upper) and simulated Lagrangian LSP velocities v (lower), subdivided in cylindrical coordinates z (height), r (radial) and θ (azimuthal) for $n = 55$ rpm for the sensitivity study. Both particle types are simultaneous in the STR. PDFs are offset for clarity. All velocities are normalized by their respective rms value from a separate undisturbed tracer simulation (dashed line).

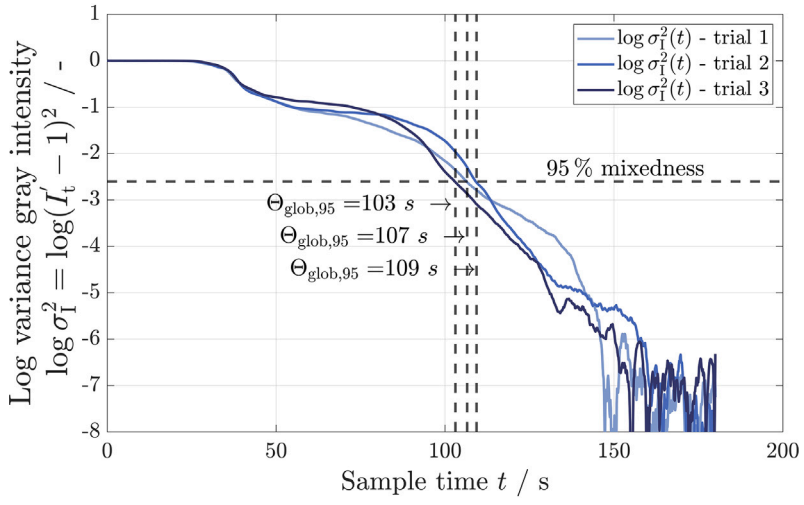

Fig. 19. Logarithmic variance of the normalized gray scale intensity $\log \sigma_I^2$ as a function of the sample time t for three trials at 55 rpm. Resulting time $\Theta_{glob,95}$ reveals the global mixing time at a 95% mixedness [74].

References

[1] S. Schwarz, T. Frey, M. Hoffmann, M. Grünewald, M. Schlüter, CFD-based compartment modeling of continuous polymer reactors in milli-structured apparatuses by use of the mean age theory, Ind. Eng. Chem. Res. 62 (31) (2023) 12109–12119, http://dx.doi.org/10.1021/acs.iecr.3c00947.

[2] M. Kuschel, F. Siebler, R. Takors, Lagrangian trajectories to predict the formation of population heterogeneity in large-scale bioreactors, Bioengineering 4 (4) (2017) 27, http://dx.doi.org/10.3390/bioengineering4020027.

[3] S. Lieder, M. Jahn, J. Koepff, S. Müller, R. Takors, Environmental stress speeds up DNA replication in Pseudomonas putida in chemostat cultivations, Biotechnol. J. 11 (1) (2016) 155–163, http://dx.doi.org/10.1002/biot.201500059.

[4] C. Haringa, H.J. Noorman, R.F. Mudde, Lagrangian modeling of hydrodynamic–kinetic interactions in (bio)chemical reactors: Practical implementation and setup guidelines, Chem. Eng. Sci. 157 (2017) 159–168, http://dx.doi.org/10.1016/j.ces.2016.07.031.

[5] A.-L. Heins, D. Weuster-Botz, Population heterogeneity in microbial bioprocesses: Origin, analysis, mechanisms, and future perspectives, Bioprocess Biosyst. Eng. 41 (7) (2018) 889–916, http://dx.doi.org/10.1007/s00449-018-1922-3.

[6] G. Wang, W. Tang, J. Xia, J. Chu, H. Noorman, W.M. van Gulik, Integration of microbial kinetics and fluid dynamics toward model-driven scale-up of industrial bioprocesses, Eng. Life Sci. 15 (1) (2015) 20–29, http://dx.doi.org/10.1002/elsc.201400172.

[7] A.R. Lara, E. Galindo, O.T. Ramírez, L.A. Palomares, Living with heterogeneities in bioreactors: understanding the effects of environmental gradients on cells, Mol. Biotechnol. 34 (3) (2006) 355–382, http://dx.doi.org/10.1385/MB:34:3:355.

[8] M. Kuschel, J. Wutz, M. Salli, D. Monteil, T. Wucherpfennig, CFD supported scale up of perfusion bioreactors in biopharma, Front. Chem. Eng. 5 (2023) 1076509, http://dx.doi.org/10.3389/fceng.2023.1076509.

[9] F. Mittermeier, M. Bäumler, P. Arulrajah, J.d. García Lima, S. Hauke, A. Stock, D. Weuster-Botz, Artificial microbial consortia for bioproduction processes, Eng. Life Sci. 23 (1) (2023) e2100152, http://dx.doi.org/10.1002/elsc.202100152.

[10] F. Kratzl, A. Kremling, K. Pflüger-Grau, Streamlining of a synthetic co-culture towards an individually controllable one-pot process for polyhydroxyalkanoate production from light and CO2, Eng. Life Sci. 23 (1) (2023) e2100156, http://dx.doi.org/10.1002/elsc.202100156.

[11] J. Herzog, A. Mook, L. Guhl, M. Bäumler, M.H. Beck, D. Weuster-Botz, F.R. Bengelsdorf, A.-P. Zeng, Novel synthetic co-culture of Acetobacterium woodii and Clostridium drakei using CO2 and in situ generated H2 for the production of caproic acid via lactic acid, Eng. Life Sci. 23 (1) (2023) e2100169, http://dx.doi.org/10.1002/elsc.202100169.

[12] A. Mook, J. Herzog, P. Walther, P. Dürre, F.R. Bengelsdorf, Lactate-mediated mixotrophic co-cultivation of Clostridium drakei and recombinant Acetobacterium woodii for autotrophic production of volatile fatty acids, Microb. Cell Factories 23 (1) (2024) 213, http://dx.doi.org/10.1186/s12934-024-02481-3.

[13] O. Š.rom, M. Š.oóš, M. Kuschel, T. Wucherpfennig, J. Fitschen, M. Schlüter, Study of hydrodynamic stress in cell culture bioreactors via lattice-Boltzmann CFD simulations supported by micro-probe shear stress method, Biochem. Eng. J. 208 (2024) 109337, http://dx.doi.org/10.1016/j.bej.2024.109337.

[14] A.W. Nienow, The impact of fluid dynamic stress in stirred bioreactors – the scale of the biological entity: a personal view, Chem. Ing. Tech. 93 (1–2) (2021) 17–30, http://dx.doi.org/10.1002/cite.202000176.

[15] F. Siebler, A. Lapin, M. Hermann, R. Takors, The impact of CO gradients on C. Ljungdahlii in a 125 M3 bubble column: Mass transfer, circulation time and lifeline analysis, Chem. Eng. Sci. 207 (2019) 410–423, http://dx.doi.org/10.1016/j.ces.2019.06.018.

[16] C. Haringa, W. Tang, A.T. Deshmukh, J. Xia, M. Reuss, J.J. Heijnen, R.F. Mudde, H.J. Noorman, Euler-Lagrange computational fluid dynamics for (bio)reactor scale down: An analysis of organism lifelines, Eng. Life Sci. 16 (7) (2016) 652–663, http://dx.doi.org/10.1002/elsc.201600061.

[17] G. Nadal-Rey, J.M. Kavanagh, B. Cassells, S. Cornelissen, D.F. Fletcher, K.V. Gernaey, D.D. McClure, Modelling of industrial-scale bioreactors using the particle lifeline approach, Biochem. Eng. J. 198 (2023) 108989, http://dx.doi.org/10.1016/j.bej.2023.108989.

[18] P. Neubauer, S. Junne, Scale-down simulators for metabolic analysis of large-scale bioprocesses, Curr. Opin. Biotechnol. 21 (1) (2010) 114–121, http://dx.doi.org/10.1016/j.copbio.2010.02.001.

[19] L. Gaugler, S. Hofmann, M. Schlüter, R. Takors, Mimicking CHO large-scale effects in the single multicompartment bioreactor: A new approach to access scale-up behavior, Biotechnol. Bioeng. (2024) http://dx.doi.org/10.1002/bit.28647.

[20] L. Gaugler, Y. Mast, J. Fitschen, S. Hofmann, M. Schlüter, R. Takors, Scaling-down biopharmaceutical production processes via a single multi-compartment bioreactor (SMCB), Eng. Life Sci. (2022) http://dx.doi.org/10.1002/elsc.202100161, elsc.202100161.

[21] L. Blöbaum, L. Torello Pianale, L. Olsson, A. Grünberger, Quantifying microbial robustness in dynamic environments using microfluidic single-cell cultivation, Microb. Cell Factories 23 (1) (2024) 44, http://dx.doi.org/10.1186/s12934-024-02318-z.

[22] Y. Liao, D. Lucas, A literature review of theoretical models for drop and bubble breakup in turbulent dispersions, Chem. Eng. Sci. 64 (15) (2009) 3389–3406, http://dx.doi.org/10.1016/j.ces.2009.04.026.

[23] Y. Liao, D. Lucas, A literature review on mechanisms and models for the coalescence process of fluid particles, Chem. Eng. Sci. 65 (10) (2010) 2851–2864, http://dx.doi.org/10.1016/j.ces.2010.02.020.

[24] C. Weiland, A. von Kameke, M. Schlüter, Trajectory-based breakup modelling for dense bubbly flows, Chem. Eng. J. 499 (2024) 155726, http://dx.doi.org/10.1016/j.cej.2024.155726.

[25] E. Anane, I.M. Knudsen, G.C. Wilson, Scale-down cultivation in mammalian cell bioreactors—The effect of bioreactor mixing time on the response of CHO cells to dissolved oxygen gradients, Biochem. Eng. J. 166 (2021) 107870, http://dx.doi.org/10.1016/j.bej.2020.107870.

[26] A. Janoska, J.J. Verheijen, W. Tang, Q. Lee, B. Sikkema, W.M. van Gulik, Influence of oxygen concentration on the metabolism of Penicillium chrysogenum, Eng. Life Sci. 23 (1) (2023) e2100139, http://dx.doi.org/10.1002/elsc.202100139.

[27] J. Bisgaard, M. Muldbak, S. Cornelissen, T. Tajsoleiman, J.K. Huusom, T. Rasmussen, K.V. Gernaey, Flow-following sensor devices: A tool for bridging data and model predictions in large-scale fermentations, Comput. Struct. Biotechnol. J. 18 (2020) 2908–2919, http://dx.doi.org/10.1016/j.csbj.2020.10.004.

[28] S. Reinecke, A. Deutschmann, K. Jobst, H. Kryk, E. Friedrich, U. Hampel, Flow following sensor particles—Validation and macro-mixing analysis in a stirred fermentation vessel with a highly viscous substrate, Biochem. Eng. J. 69 (2012) 159–171, http://dx.doi.org/10.1016/j.bej.2012.09.010.

[29] L. Buntkiel, Y. Ma, S.F. Reinecke, U. Hampel, Orientation resolved measurements of accelerations with sensor particles in bioreactors, Tm - Tech. Mess. 90 (12) (2023) 835–845, http://dx.doi.org/10.1515/teme-2023-0115.

[30] A. Lapin, D. Müller, M. Reuss, Dynamic behavior of microbial populations in stirred bioreactors simulated with Euler-Lagrange methods: Traveling along the lifelines of single cells, Ind. Eng. Chem. Res. 43 (16) (2004) 4647–4656, http://dx.doi.org/10.1021/ie030786k.

[31] L. Blöbaum, C. Haringa, A. Grünberger, Microbial lifelines in bioprocesses: From concept to application, Biotech. Adv. 62 (2023) 108071, http://dx.doi.org/10.1016/j.biotechadv.2022.108071.

[32] S. Hofmann, L. Buntkiel, R. Rautenbach, L. Gaugler, Y. Ma, I. Haase, J. Fitschen, T. Wucherpfennig, S. Reinecke, M. Hoffmann, R. Takors, U. Hampel, M. Schlüter, Experimental analysis of lifelines in a 15,000 L bioreactor by means of Lagrangian Sensor Particles, Chem. Eng. Res. Des. 205 (2024) 695–712, http://dx.doi.org/10.1016/j.cherd.2024.04.015.

[33] R. Rautenbach, S. Hofmann, L. Buntkiel, J. Schäfer, S.F. Reinecke, M. Hoffmann, U. Hampel, M. Schlüter, Dynamics of Lagrangian sensor particles: the effect of non-homogeneous mass distribution, Processes 12 (8) (2024) 1617, http://dx.doi.org/10.3390/pr12081617.

[34] S. Hofmann, C. Weiland, J. Fitschen, A. von Kameke, M. Hoffmann, M. Schlüter, Lagrangian sensors in a stirred tank reactor: Comparing trajectories from 4D-particle tracking velocimetry and Lattice-Boltzmann simulations, 137549, Chem. Eng. J. 449 (2022) 22, http://dx.doi.org/10.1016/j.cej.2022.137549.

[35] L. Buntkiel, S.F. Reinecke, U. Hampel, Beschleunigungsmessung als Grundlage für die Strömungsverfolgung in Bioreaktoren mit Sensorpartikeln: Acceleration measurement for flow tracking in bioreactors with sensor particles, Tm - Tech. Mess. 90 (s1) (2023) 43–48, http://dx.doi.org/10.1515/teme-2023-0078.

[36] L. Buntkiel, S. Reinecke, A. Heller, C. Budelmann, U. Hampel, Mit UWB-Lokalisierung gekoppelte inertiale Lage- und Bewegungsverfolgung für instrumentierte Strömungsfolger, in: Vorträge, AMA Service GmbH, Von-Münchhausen-Str. 49, 31515 Wunstorf, Germany, 2021, pp. 22–27, http://dx.doi.org/10.5162/15dss2021/2.2, Online.

[37] J. Kersebaum, S. Flaischlen, J. Hofinger, G.D. Wehinger, Simulating stirred tank reactor characteristics with a lattice Boltzmann CFD code, Chem. Eng. Technol. 47 (3) (2024) 586–595, http://dx.doi.org/10.1002/ceat.202300384.

[38] J.A. Thomas, B. DeVincentis, E. Janz, B. Turner, A general approach for predicting convective heat transfer coefficients in turbulent systems, Int. J. Heat Mass Transfer 220 (2024) 124989, http://dx.doi.org/10.1016/j.ijheatmasstransfer.2023.124989.

[39] J. Thomas, K. Sinha, G. Shivkumar, L. Cao, M. Funck, S. Shang, N.K. Nere, A CFD digital twin to understand miscible fluid blending, AAPS PharmSciTech 22 (3) (2021) 91, http://dx.doi.org/10.1208/s12249-021-01972-5.

[40] M. Kuschel, J. Fitschen, M. Hoffmann, A. von Kameke, M. Schlüter, T. Wucherpfennig, Validation of novel lattice Boltzmann large eddy simulations (LB LES) for equipment characterization in biopharma, Processes 9 (6) (2021) 950, http://dx.doi.org/10.3390/pr9060950.

[41] Z.-G. Feng, E.E. Michaelides, The immersed boundary-lattice Boltzmann method for solving fluid–particles interaction problems, J. Comput. Phys. 195 (2) (2004) 602–628, http://dx.doi.org/10.1016/j.jcp.2003.10.013.

[42] M-Star Simulations, LLC, M-Star CFD Documentation, 2024, https://docs.mstarcfd.com/.

[43] A. Rosseburg, J. Fitschen, J. Wutz, T. Wucherpfennig, M. Schlüter, Hydrodynamic inhomogeneities in large scale stirred tanks – Influence on mixing time, Chem. Eng. Sci. 188 (2018) 208–220, http://dx.doi.org/10.1016/j.ces.2018.05.008.

[44] E. Ståhl Wernersson, C. Trägårdh, Scale-up of Rushton turbine-agitated tanks, Chem. Eng. Sci. 54 (19) (1999) 4245–4256, http://dx.doi.org/10.1016/S0009-2509(99)00127-X.

[45] A.W. Nienow, B. Isailovic, T.A. Barrett, Design and performance of single-use, stirred-tank bioreactors, Bioprocess Int. 14 (10) (2016) 12–21.

[46] A. Nienow, K. Coopman, T. Heathman, Q. Rafiq, C. Hewitt, Bioreactor engineering fundamentals for stem cell manufacturing, in: Stem Cell Manufacturing, Elsevier, 2016, pp. 43–75, http://dx.doi.org/10.1016/B978-0-444-63265-4.00003-0.

[47] G.I. Taylor, Statistical theory of turbulence, in: Proceedings of the Royal Society of London. Series a - Mathematical and Physical Sciences, 873, Vol. 151, The Royal Society, 1935, pp. 421–444, http://dx.doi.org/10.1098/rspa.1935.0158.

[48] D.G.F. Huilier, An overview of the Lagrangian dispersion modeling of heavy particles in homogeneous isotropic turbulence and considerations on related LES simulations, Fluids 6 (4) (2021) 145, http://dx.doi.org/10.3390/fluids6040145.

[49] TE Connectivity, Datasheet 9mm Digital Output Pressure Sensor 89BSD-006BA-A, 2019.

[50] C.T. Crowe, J.D. Schwarzkopf, M. Sommerfeld, Y. Tsuji, Multiphase Flows with Droplets and Particles, second ed., CRC Press, 2011, http://dx.doi.org/10.1201/b11103.

[51] J.K. Eaton, J.R. Fessler, Preferential concentration of particles by turbulence, Int. J. Multiph. Flow 20 (1994) 169–209, http://dx.doi.org/10.1016/0301-9322(94)90072-8.

[52] N.T. Ouellette, P.J.J. O'Malley, J.P. Gollub, Transport of finite-sized particles in chaotic flow, Phys. Rev. Lett. 101 (17) (2008) 174504, http://dx.doi.org/10.1103/PhysRevLett.101.174504.

[53] C. Tropea, A.L. Yarin, J.F. Foss (Eds.), Springer Handbook of Experimental Fluid Mechanics, Springer, Berlin, 2007.

[54] A. Haider, O. Levenspiel, Drag coefficient and terminal velocity of spherical and nonspherical particles, Powder Technol. 58 (1) (1989) 63–70, http://dx.doi.org/10.1016/0032-5910(89)80008-7.

[55] M.R. Maxey, J.J. Riley, Equation of motion for a small rigid sphere in a nonuniform flow, Phys. Fluids 26 (4) (1983) 883, http://dx.doi.org/10.1063/1.864230.

[56] E. Calzavarini, R. Volk, E. Lévêque, J.-F. Pinton, F. Toschi, Impact of trailing wake drag on the statistical properties and dynamics of finite-sized particle in turbulence, Phys. D: Nonlinear Phenom. 241 (3) (2012) 237–244, http://dx.doi.org/10.1016/j.physd.2011.06.004.

[57] M. Zlokarnik, Stirring: Theory and Practice, Wiley-VCH Verlag GmbH, Weinheim, Germany, 2001.

[58] A. Ochieng, M.S. Onyango, Drag models, solids concentration and velocity distribution in a stirred tank, Powder Technol. 181 (1) (2008) 1–8, http://dx.doi.org/10.1016/j.powtec.2007.03.034.

[59] J. Fitschen, S. Hofmann, J. Wutz, A. Kameke, M. Hoffmann, T. Wucherpfennig, M. Schlüter, Novel evaluation method to determine the local mixing time distribution in stirred tank reactors, Chem. Eng. Sci.: X 10 (2021) 100098, http://dx.doi.org/10.1016/j.cesx.2021.100098.

[60] A.W. Nienow, On impeller circulation and mixing effectiveness in the turbulent flow regime, Chem. Eng. Sci. 52 (15) (1996) 2557–2565, http://dx.doi.org/10.1016/S0009-2509(97)00072-9.

[61] G. Bellani, E.A. Variano, Slip velocity of large neutrally buoyant particles in turbulent flows, New J. Phys. 14 (12) (2012) 125009, http://dx.doi.org/10.1088/1367-2630/14/12/125009.

[62] J.A. Thomas, X. Liu, B. DeVincentis, H. Hua, G. Yao, M.C. Borys, K. Aron, G. Pendse, A mechanistic approach for predicting mass transfer in bioreactors, Chem. Eng. Sci. 237 (2021) 116538, http://dx.doi.org/10.1016/j.ces.2021.116538.

[63] C. Weiland, E. Steuwe, J. Fitschen, M. Hoffmann, M. Schlüter, K. Padberg-Gehle, A. von Kameke, Computational study of three-dimensional Lagrangian transport and mixing in a stirred tank reactor, Chem. Eng. J. Adv. 14 (2023) 100448, http://dx.doi.org/10.1016/j.ceja.2023.100448.

[64] S. Succi, The lattice Boltzmann equation for fluid dynamics and beyond, in: Numerical Mathematics and Scientific Computation, Clarendon Press ; Oxford University Press, Oxford, New York, 2001.

[65] Z. Guo, C. Shu, Lattice Boltzmann method and its applications in engineering, in: Advances in Computational Fluid Dynamics, (v. 3) World Scientfic, [Hackensack,] New Jersey, 2013.

[66] A.A. Mohamad, Lattice Boltzmann Method: Fundamentals and Engineering Applications with Computer Codes, Springer London, London, 2019, http://dx.doi.org/10.1007/978-1-4471-7423-3.

[67] S.B. Pope, Turbulent Flows, Cambridge University Press, Cambridge ; New York, 2000.

[68] S.F. Reinecke, Instrumentierte Strömungsfolger zur Prozessdiagnose in gerührten Fermentern (Ph.D. thesis), Dresden University of Technology, Dresden, 2013.

[69] A. Gabriele, A. Tsoligkas, I. Kings, M. Simmons, Use of PIV to measure turbulence modulation in a high throughput stirred vessel with the addition of high Stokes number particles for both up- and down-pumping configurations, Chem. Eng. Sci. 66 (23) (2011) 5862–5874, http://dx.doi.org/10.1016/j.ces.2011.08.007.

[70] N.T. Ouellette, P.J.J. O'Malley, J.P. Gollub, Transport of finite-sized particles in chaotic flow, Phys. Rev. Lett. 101 (17) (2008) 174504, http://dx.doi.org/10.1103/PhysRevLett.101.174504.

[71] F. Lucci, A. Ferrante, S. Elghobashi, Is Stokes number an appropriate indicator for turbulence modulation by particles of Taylor-length-scale size? Phys. Fluids 23 (2) (2011) 025101, http://dx.doi.org/10.1063/1.3553279.

[72] M. Cisse, E.-W. Saw, M. Gibert, E. Bodenschatz, J. Bec, Turbulence attenuation by large neutrally buoyant particles, Phys. Fluids 27 (6) (2015) 061702, http://dx.doi.org/10.1063/1.4922241.

[73] G. Bellani, M.L. Byron, A.G. Collignon, C.R. Meyer, E.A. Variano, Shape effects on turbulent modulation by large nearly neutrally buoyant particles, J. Fluid Mech. 712 (2012) 41–60, http://dx.doi.org/10.1017/jfm.2012.393.

[74] E.L. Paul, V.A. Atiemo-Obeng, S.M. Kresta (Eds.), Handbook of Industrial Mixing: Science and Practice, Wiley-Interscience, Hoboken, NJ, USA, 2004.

[75] M. Cisse, H. Homann, J. Bec, Slipping motion of large neutrally buoyant particles in turbulence, J. Fluid Mech. 735 (2013) R1, http://dx.doi.org/10.1017/jfm.2013.490.

[76] J. Bisgaard, M. Muldbak, T. Tajsoleiman, T. Rydal, T. Rasmussen, J.K. Huusom, K.V. Gernaey, Characterization of mixing performance in bioreactors using flow-following sensor devices, Chem. Eng. Res. Des. 174 (2021) 471–485, http://dx.doi.org/10.1016/j.cherd.2021.08.008.

[77] K. Van't Riet, J.M. Smith, The trailing vortex system produced by Rushton turbine agitators, Chem. Eng. Sci. 30 (9) (1975) 1093–1105, http://dx.doi.org/10.1016/0009-2509(75)87012-6.

[78] T. Lauterbach, T. Lüke, M.-J. Büker, C. Hedayat, T. Gernandt, R. Moll, M. Grösel, S. Lenk, F. Seidel, D. Brunner, T. Bley, T. Walther, F. Lenk, Measurements on the fly– Introducing mobile micro-sensors for Biotechnological applications, Sensors Actuators A: Phys. 287 (2019) 29–38, http://dx.doi.org/10.1016/j.sna.2019.01.003.

[79] J. Bec, A. Celani, M. Cencini, S. Musacchio, Clustering and collisions of heavy particles in random smooth flows, Phys. Fluids 17 (7) (2005) 073301, http://dx.doi.org/10.1063/1.1940367.

[80] J. Bec, H. Homann, S.S. Ray, Gravity-driven enhancement of heavy particle clustering in turbulent flow, Phys. Rev. Lett. 112 (18) (2014) 184501, http://dx.doi.org/10.1103/PhysRevLett.112.184501.

[81] R.K. Bajpai, M. Reuss, Coupling of mixing and microbial kinetics for evaluating the performance of bioreactors, Can. J. Chem. Eng. 60 (3) (1982) 384–392, http://dx.doi.org/10.1002/cjce.5450600308.

[82] G. Ascanio, Mixing time in stirred vessels: A review of experimental techniques, Chin. J. Chem. Eng. 23 (7) (2015) 1065–1076, http://dx.doi.org/10.1016/j.cjche.2014.10.022.

[83] J.C. Middleton, Measurement of circulation within large mixing vessels, in: Proceedings of the 3rd European Conference on Mixing: Held At the University of York, Vol. 1, BHRA Fluid Engineering, Cranfield, Bedford, England, 1979, pp. 15–36.

[84] R. Mann, P. Mavros, J.C. Middleton, A structured stochastic flow model for interpreting flow-follower data from a stirred vessel, Trans. Inst. Chem. Eng. 59 (4) (1981) 271–278.

[85] A.M. Day, Mixing in Stirred Tanks (Ph.D. thesis), University of Exeter, University of Exeter, 1975.

[86] C. Haringa, An analysis of organism lifelines in an industrial bioreactor using Lattice-Boltzmann CFD, Eng. Life Sci. 23 (1) (2023) http://dx.doi.org/10.1002/elsc.202100159.

[87] M.D. Hoang, I. Polte, L. Frantzmann, N. Von Den Eichen, A.-L. Heins, D. Weuster-Botz, Impact of mixing insufficiencies on L-phenylalanine production with an Escherichia coli reporter strain in a novel two-compartment bioreactor, Microb. Cell Factories 22 (1) (2023) 153, http://dx.doi.org/10.1186/s12934-023-02165-4.

[88] R. Pörtner, J.-O. Schwabe, B. Frahm, Evaluation of selected control strategies for fed-batch cultures of a hybridoma cell line, Biotechnol. Appl. Biochem. 40 (1) (2004) 47–55, http://dx.doi.org/10.1042/BA20030168.

[89] G. Nadal-Rey, D.D. McClure, J.M. Kavanagh, B. Cassells, S. Cornelissen, D.F. Fletcher, K.V. Gernaey, Development of dynamic compartment models for industrial aerobic fed-batch fermentation processes, Chem. Eng. J. 420 (2021) 130402, http://dx.doi.org/10.1016/j.cej.2021.130402.

[90] V. Bernemann, J. Fitschen, M. Leupold, K.-H. Scheibenbogen, M. Maly, M. Hoffmann, T. Wucherpfennig, M. Schlüter, Characterization data for the establishment of scale-up and process transfer strategies between stainless steel and single-use bioreactors, Fluids 9 (5) (2024) 115, http://dx.doi.org/10.3390/fluids9050115.

[91] M. Al-Rubeai (Ed.), Animal Cell Culture, in: Cell Engineering, vol. 9, Springer International Publishing, Cham, 2015, http://dx.doi.org/10.1007/978-3-319-10320-4.

[92] L. Böhm, L. Hohl, C. Bliatsiou, M. Kraume, Multiphase stirred tank bioreactors – new geometrical concepts and scale-up approaches, Chem. Ing. Tech. 91 (12) (2019) 1724–1746, http://dx.doi.org/10.1002/cite.201900165.
[93] M. Bartczak, M. Pilarek, The colourimetric method for mixing time measurement in single-use and multi-use bioreactors—methodology overview and practical recommendations, Energies 17 (1) (2024) 221, http://dx.doi.org/10.3390/en17010221.
[94] M. Cooke, J.C. Middleton, J.R. Bush, Mixing and mass transfer in filamentous fermentations, in: 2nd International Conference on Bioreactor Fluid Dynamics, Cranfield, UK, 1988, pp. 37–64.
[95] C. Sieblist, M. Jenzsch, M. Pohlscheidt, Equipment characterization to mitigate risks during transfers of cell culture manufacturing processes, Cytotechnology 68 (4) (2016) 1381–1401, http://dx.doi.org/10.1007/s10616-015-9899-0.
[96] J.M. Vasconcelos, S. Alves, J.M. Barata, Mixing in gas-liquid contactors agitated by multiple turbines, Chem. Eng. Sci. 50 (14) (1995) 2343–2354, http://dx.doi.org/10.1016/0009-2509(95)00090-R.
[97] S.J. Khang, O. Levenspiel, New scale-up and design method for stirrer agitated batch mixing vessels, Chem. Eng. Sci. 31 (7) (1976) 569–577, http://dx.doi.org/10.1016/0009-2509(76)80020-6.
[98] R. Voncken, D. Holmes, H. Den Hartog, Fluid flow in turbine-stirred, baffled tanks—II, Chem. Eng. Sci. 19 (3) (1964) 209–213, http://dx.doi.org/10.1016/0009-2509(64)85031-4.
[99] D. Holmes, R. Voncken, J. Dekker, Fluid flow in turbine-stirred, baffled tanks—I, Chem. Eng. Sci. 19 (3) (1964) 201–208, http://dx.doi.org/10.1016/0009-2509(64)85030-2.
[100] J.G. van de Vusse, A new model for the stirred tank reactor, Chem. Eng. Sci. 17 (7) (1962) 507–521, http://dx.doi.org/10.1016/0009-2509(62)87002-X.
[101] M. Kraume, P. Zehner, Experience with experimental standards for measurements of various parameters in stirred tanks: a comparative test, Chem. Eng. Res. Des. 79 (8) (2001) http://dx.doi.org/10.1205/02638760152721316.
[102] H.-J. Henzler, Rührprobleme in der Biotechnologie, in: Mischen Und Rühren, John Wiley & Sons, Ltd, 2002, pp. 375–403, http://dx.doi.org/10.1002/3527603360.ch15.
[103] A.W. Nienow, C. Langheinrich, N.C. Stevenson, A.N. Emery, T.M. Clayton, N.K.H. Slater, Homogenisation and oxygen transfer rates in large agitated and sparged animal cell bioreactors: Some implications for growth and production, Cytotechnology 22 (1) (1996) 87–94, http://dx.doi.org/10.1007/BF00353927.
[104] J.-C. Gabelle, F. Augier, A. Carvalho, R. Rousset, J. Morchain, Effect of tank size on kLa and mixing time in aerated stirred reactors with non-Newtonian fluids, Can. J. Chem. Eng. 89 (5) (2011) 1139–1153, http://dx.doi.org/10.1002/cjce.20571.
[105] F. Magelli, G. Montante, D. Pinelli, A. Paglianti, Mixing time in high aspect ratio vessels stirred with multiple impellers, Chem. Eng. Sci. 101 (2013) 712–720, http://dx.doi.org/10.1016/j.ces.2013.07.022.
[106] A.W. Nienow, Hydrodynamics of stirred bioreactors, Appl. Mech. Rev. 51 (1) (1998) 3–32, http://dx.doi.org/10.1115/1.3098990.
[107] J. Fitschen, (Ph.D. thesis), Hamburg University of Technology, Institute of Multiphase Flows, 2021.
[108] M. Manikowski, S. Bodemeier, A. Lübbert, W. Bujalski, A.W. Nienow, Measurement of gas and liquid flows in stirred tank reactors with multiple agitators, Can. J. Chem. Eng. 72 (5) (1994) 769–781, http://dx.doi.org/10.1002/cjce.5450720502.
[109] M. Kuschel, R. Takors, Simulated oxygen and glucose gradients as a prerequisite for predicting industrial scale performance *a Priori*, Biotechnol. Bioeng. 117 (9) (2020) 2760–2770, http://dx.doi.org/10.1002/bit.27457.
[110] S.F. Wright, I. Zadrazil, C.N. Markides, A review of solid–fluid selection options for optical-based measurements in single-phase liquid, two-phase liquid–liquid and multiphase solid–liquid flows, Exp. Fluids 58 (9) (2017) 108, http://dx.doi.org/10.1007/s00348-017-2386-y.
[111] A.R. Lara, L.A. Palomares, O.T. Ramírez, Scale-down: simulating large-scale cultures in the laboratory, in: Industrial Biotechnology, John Wiley & Sons, Ltd, 2017, pp. 55–79, http://dx.doi.org/10.1002/9783527807833.ch2.
[112] G. Nadal-Rey, D.D. McClure, J.M. Kavanagh, S. Cornelissen, D.F. Fletcher, K.V. Gernaey, Understanding gradients in industrial bioreactors, Biotech. Adv. 46 (2021) 107660, http://dx.doi.org/10.1016/j.biotechadv.2020.107660.
[113] J. Zhao, M.A. Muawiya, Y. Zhuang, G. Wang, Developing rational scale-down simulators for mimicking substrate heterogeneities based on cell lifelines in industrial-scale bioreactors, Bioresour. Technol. 395 (2024) 130354, http://dx.doi.org/10.1016/j.biortech.2024.130354.
[114] P. Ho, S. Täuber, B. Stute, A. Grünberger, E. von Lieres, Microfluidic reproduction of dynamic bioreactor environment based on computational lifelines, Front. Chem. Eng. 4 (2022) 826485, http://dx.doi.org/10.3389/fceng.2022.826485.
[115] C. Haringa, R.F. Mudde, H.J. Noorman, From industrial fermentor to CFD-guided downscaling: What have we learned? Biochem. Eng. J. 140 (2018) 57–71, http://dx.doi.org/10.1016/j.bej.2018.09.001.
[116] C. Haringa, A.T. Deshmukh, R.F. Mudde, H.J. Noorman, Euler-Lagrange analysis towards representative down-scaling of a 22 m 3 aerobic S. Cerevisiae fermentation, Chem. Eng. Sci. 170 (2017) 653–669, http://dx.doi.org/10.1016/j.ces.2017.01.014.
[117] E.W. Saw, R.A. Shaw, S. Ayyalasomayajula, P.Y. Chuang, Á. Gylfason, Inertial clustering of particles in high-Reynolds-number turbulence, Phys. Rev. Lett. 100 (21) (2008) 214501, http://dx.doi.org/10.1103/PhysRevLett.100.214501.
[118] H. Brauer, D. Mewes, Strömungswiderstand sowie stationärer und instationärer Stoff- und Wärmeübergang an Kugeln: Strömungswiderstand sowie stationärer und instationärer Stoff- und Wärmeübergang an Kugeln, Chem. Ing. Tech. 44 (13) (1972) 865–868, http://dx.doi.org/10.1002/cite.330441314.